UNIVERSITÀ DEGLI STUDI DI CATANIA
DOTTORATO DI RICERCA IN SCIENZA DEI MATERIALI
XXIII CICLO

Dr. GIACOMO PATANE'

Production and characterization of Carbon based and inorganic nanostructures

Tutor:
Prof. ORAZIO PUGLISI

Coordinatore:
Prof. ANTONINO LICCIARDELLO

ANNO ACCADEMICO 2009 – 2010

Stat rosa pristina nomine, nomina nuda tenemus

U. Eco, “Il nome della rosa”

Index

Ringraziamenti

Desidero ringraziare il mio Tutor Prof. Orazio Puglisi per la possibilità fornitami di svolgere il mio dottorato all'interno del suo gruppo di ricerca. Lo ringrazio per avermi sempre garantito un supporto scientifico di elevatissima qualità e per avermi saputo trasmettere la passione per la ricerca e la capacità di inquadrare i fenomeni secondo metodologie rigorose.

Ringrazio il Prof. Giuseppe Compagnini per avermi sempre coinvolto appieno nelle tematiche scientifiche che abbiamo trattato insieme, non solo come un semplice "esecutore di misure", ma come scienziato in grado di studiare integralmente una tematica di ricerca, sia dal punto di vista teorico che sperimentale. Lo ringrazio inoltre per avermi voluto coinvolgere come parte attiva in progetti ed in collaborazioni con altri gruppi di ricerca, anche stranieri, con i quali ho avuto modo di svolgere un lavoro estremamente interessante e di elevata qualità scientifica.

Ringrazio la Dott. Luisa D'Urso per la simpatia e l'amicizia sempre dimostrate e per i suoi utili consigli professionali ed umani spesso dispensati.

Ringrazio inoltre i miei "compagni d'avventura" Elena Messina, Gabriele Messina e Marco Sinatra per la sincera amicizia che mi hanno donato e per tutti i momenti che hanno voluto condividere con me, creando un ambiente sereno che ha reso più piacevoli le lunghe ore di lavoro trascorse.

Ringrazio il Sig. Giuseppe Indelli del Consorzio Catania Ricerche, per la continua e pronta assistenza tecnica fornitami e per la disponibilità sempre dimostrata.

Ringrazio il personale dell'IMETEM, in particolare il Sig. Corrado Bongiorno per l'assistenza fornita durante l'esecuzione delle misure al TEM ed il Sig. Antonio La Mantia della STMicroelectronics per l'esecuzione delle misure al SEM.

Preface

Since its appearance on Earth, man has tried to change the environment so as to make it more suitable to his lifestyle needs. To this purpose he has always used the materials at his disposal for the creation of various tools, not by chance that the major eras of ancient history are marked by the name of the most widely used in that period. Prehistoric eras are classified, according to a periodization method designed by the Danish scientist Thomsen, from the Stone Age to the Bronze Age to the Iron Age. The change in production systems used and the development of new methods of production has been very heavy political and social repercussions on the organization leading the transition to forms of social structure gradually more complex.

More recently, in conjunction with the advent of the industrial revolution in the nineteenth century, there has been a real explosion in the production of a wide range of new materials, mainly due to the discovery of polymeric materials and to the possibility to work petroleum to obtain its derivatives; the modern world as we know it is the product of scientific discoveries and technological applications developed in a fertile period from the mid-nineteenth century onwards.

Far from being exhausted, the drive to search for new materials continues its run exponentially today thanks to the discovery of a new and interesting field of research which is that of nanomaterials. Born with the discovery of fullerenes in 1985 by Kroto [1], the study of nanomaterials has continued with increasing speed up to the discovery of carbon nanotubes by Ijima in 1991[2], which can

be considered a milestone in this field of research. Today it is possible to produce a huge range of nanomaterials, ranging from the aforementioned fullerenes and carbon nanotubes with inorganic nanowires, metal nanoparticles, graphene, to mention only the main classes. In addition, the production of nanocomposites by combining together different nanostructures or by producing them in a single step, allows to obtain new materials with the desired properties for specific applications.

This scenario opens new frontiers in the development of innovative materials for targeted applications in various fields of human activity.

The dramatic development which has taken place in the recent years in the production of nanostructures has been made possible by the simultaneous development of adequate tools for analyzing chemical and physical materials involved, and particularly their surfaces.

The knowledge of the chemical and structural properties of the surface of nanomaterials is indeed of paramount importance as these objects, just because of their small size, have a very high surface / volume ratio and their optical and electronic properties are determined by chemical and physical characteristics of their surfaces.

I used spectroscopic tools like X-rays Photoelectron Spectroscopy (XPS) and Raman Spectroscopy, together with UV-VIS spectrometer, to characterize the chemical nature of the nanomaterials produced. I also used microscopic techniques such as Scanning Electron Microscopy and Transmission Electron

Microscopy in order to define the morphological and structural nature of the samples.

The photoelectron spectroscopy is a technique capable of providing a contribution of fundamental importance in this field since it allows a complete physical and chemical characterization of nanomaterials under study. Raman spectroscopy also allows to obtain informations about the crystallinity of a given sample and is one of the main tool used for the study of carbon nanostructures as it allows to distinguish their different vibrational states . The use of these techniques, together with other integrated techniques such as SEM, TEM and AFM microscopy, allows a complete of a material in a comprehensive manner, both in terms of chemical analysis and for the morphological and structural point of view.

The work I have done during my Ph.D. research has been directed towards the study of different classes of nanomaterials both in relation with their production routes and with the characterization techniques.

Aim of the work

During my Ph.D. thesis I studied several nanostructured materials from an experimental point of view.

In particular, I took care of the spectroscopic and microscopic characterization of carbon-based nanostructures and "inorganic" nanostructure, referring by the use of this tem to nanostructures that do not contain carbon atoms.

I report here the study of six classes of the main protagonists of this fascinating world of nanomaterials, i.e. carbon nanotubes, carbon nanowires, highly oriented pyrolytic graphite (HOPG) and graphene and inorganic nanomaterials such as MoSI nanowires and MoS_2 fullerene-like (IF-MoS_2) nanostructures.

In some cases I also was involved in the production routes to obtain new classes of nanocompounds; this was the case of the laser ablation of a MoS_2 target in water to produce IF-MoS_2 structures or the production of nanocomposites between MoSI nanowires and gold nanoparticles produced by laser ablation in liquid.

The carbon-based 1-d nanomaterials, as I discuss in the following, are today among the most interesting nanostructures in Materials Science for their peculiar properties and for the huge possibilities of applications they present. In order to obtain a full comprehension of their spectroscopic properties, I considered the experimental characterization of their "precursors", i.e. HOPG and, mainly, graphene, as an important starting point.

The inorganic nanomaterials are emerging today as innovative and valuable products with very wide fields of applications, as I discuss in details on the following.

In particular, I characterized spectroscopically MoSI nanowires with two different stoichiometries and I produced and characterize a nanonetwork between these systems and gold nanoparticles produced by laser ablation in liquid.

The chemistry of Mo-S bond was also studied in IF-MoS_2, that have been produced by laser ablation in liquid and characterized by spectroscopic and microscopic techniques; in my study, I propose a possible pathway for the reactions leading to the IF-MoS_2 formation in the plasma generated by the laser ablation of the MoS_2 target.

Instrumentations

XPS Spectrometer

XPS spectrometer I used in my work is the Kratos Axis Ultra model. The X-ray radiation was generated by an Al Kα line decay (1486 eV) at operating conditions of 10 KV and 15 mA. The emitted photoelectrons were analyzed with a hemispherical electron energy analyzer. The detailed spectra have been acquired with a resolution below 1 eV.

The Survey spectra have been acquired with a step of 1 eV and an acquisition time of 150 msec per point. The high resolution spectra

of the characteristic features have been acquired with steps of 0.025 eV and an acquisition time of 300 msec per each point.

The XPS Spectrometer was upgraded by installing an electron gun in the prechamber; this upgrading allows to deposit thin films on a substrate by a technique called Pulsed Plasma Deposition, in which high energy (~ 15 keV) pulsed electrons are sent against a rotating target inside the prechamber at ~ 10-5 Torr and the ablated material is deposited on a proper substrate.

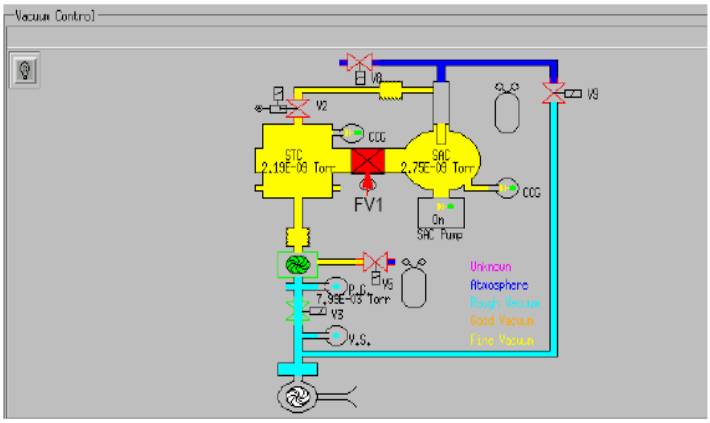

Fig. 1: Scheme of the XPS spectrometer. The STC (prechamber) and SAC (analysis chamber) are clearly visible. The pressure value in the SAC is between 10-9 – 10-10 Torr.

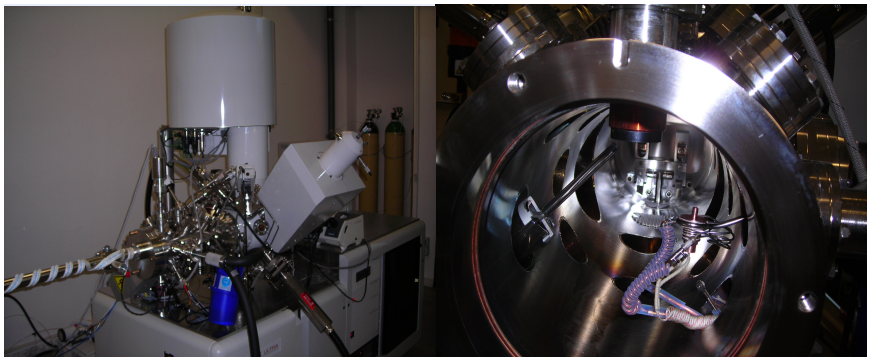

(a) (b)

Fig. 2 : Image of the XPS spectrometer, with the monochromator and the energy selector well visible (a). Image of the prechamber where the electron gun is visible on the left part of the image, while the rotating target is visible on the upper part at a distance of ~ 2 cm from the gun (b).

Raman Spectrometer

Raman spectra have been excited both by the 514.5 nm radiation of an Ar ion laser and the 632.8 nm of a He-Ne one in backscattering geometry. The backscattered light has been analyzed by a Jobin Yvon 450 mm monochromator, equipped with a CCD detector cooled with liquid nitrogen.

SEM, TEM and AFM Microscopes

Scanning Electron Microscopy (SEM) and Transmission Electron Microscopy (TEM) are the most common microscopy techniques used in the study of the morphology and structure of surfaces and nanomaterials.

In the use of SEM the sample surface is examined, while TEM is a bulk technique, since the electron beam passes through the sample this limits its application to very thin samples.

Both techniques are often coupled with analytical techniques that exploit the emitted X-rays.

In the study of nanomaterials, the Transmission Electron Microscopy can be employed to inspect the particle size distribution with resolution of several Angstroms. A Jeol 200 kV TEM microscope was used to obtain the images shown in this thesis.

Much better resolution can be obtained with a scanning probe technique such as Atomic Force Microscope (AFM).In this technique the interaction between anatomically sharp tip and the surface of a sample is measured; a very high resolution, up to atomic scale, can be reached.

In AFM tips are made of SiN3 or Si and can be maintained either at constant force from the sample surface, obtaining height information, or at constant height, obtaining force information. The tip is attached to the underside of a reflective cantilever, and a diode laser is focused onto the back of the cantilever. As tips scan the sample surface, moving up and down, following the contour of the surface, the laser beam is deflected into a dual element photo-diode.

The difference in light intensities between the two photodetectors is converted to voltage. A feedback signal through software control enables the tip to maintain either a constant force (a piezo electric transducer monitors height deviation) or a constant distance from the sample surface (the deflection force is recorded).

Three dimensional topographical maps of the surface are then constructed by plotting the local sample height vs the horizontal tip position. A nominal 5 nm lateral and 0.01 nm vertical resolution is obtained on all types of samples.

AFM can be used in three modes. In *contact mode* the tip scans the sample in close contact with the surface, and the force between the tip and the sample is repulsive.

In *non-contact mode*the tip hoves 50-150 A above the surface. Attractive van der Waals forces between the tip and the sample are detected, and the topography images are constructed by scanning the tip above the surface. Theattractive forces are weaker then the repulsive ones used in contact mode, therefore it is necessary to give the tip a small oscillation.

Tapping mode is the most recent technique and allows also the examination of surfaces poorly damaged. The tip is alternatively placed in contact with the sample surface. This enables to provide high resolution avoiding dragging the tuip across the surface. Selection of the optimal oscillation frequency is software assisted and the force on the sample is maintained at the lowest possible level.

A AFM-Digital Instrument Nanoscope, model III was used for the atomic force microscopy measurements.

Chapter 1 . Nanostructured materials: an overview

Materials science had a strong enhancement in the last two decades, with the study of nanomaterials. Nanodimensionality gives a material peculiar properties that are very often completely different from those observed for the bulk; in fact, when a material reaches the size of the order of nanometers is observed a sharp increase in surface to volume ratio and its properties become only a function of the size and shape of crystals. This leads to drastic changes in electronic properties of the material [3]. Semiconductor materials, for example, vary their electronic band structure when changing their dimensions going from a broad band to discrete energy levels [4].

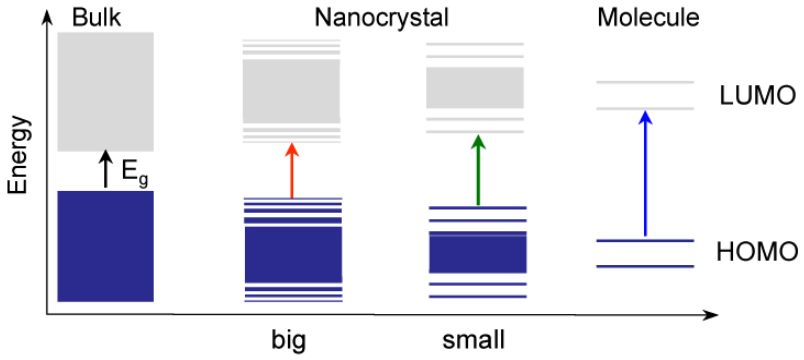

Fig. 3: Electronic band structures of a given material as a function of its dimensions

It is clear from the figure that the band gap increases with decreasing size of the material, leading to a change in the redox properties of the material.

The nanostructured materials are classified into zero, 1 or 2 dimensions [5]. Fullerene is an example of a nanostructure to zero size, or point, while polyynes, carbon nanotubes or inorganic nanowires belong to the class of 1-dimensional nanostructures and, finally, graphene can be an example of two-dimensional nanostructure [6,7].

I will hereinafter describe in details the various classes of nanomaterials so far mentioned.

1.1 Carbon Nanotubes

Carbon nanotubes, as already mentioned, can be viewed as a C sp^2 sheet folded in a cylindrical shape.

They can be divided into two main classes, single (SWCNTs) and multiwall carbon nanotubes (MWCNTs); in the first case, the material can be viewed as the result of the folding of a single sp^2 carbon sheet [8]. These structures have a diameter ranging from 0.8 to 2 nm about while their length can reach several microns. Multiwall carbon nanotubes are composed by several coaxial SWCNTs having different diameters with an interlayer spacing of 0.34 – 0.36 nm that is close to the typical spacing of turbostratic graphite and can reach a mean diameter of several tens of nm, depending on the number of single walls they include [9].

The properties of carbon nanotubes are strictly depending on their chirality; three different chiral structures are known, armchair, zigzag and chiral [10].

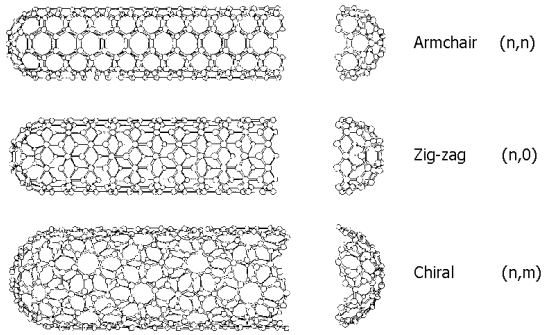

Fig. 4:Models of different single wall nanotubes (Saito et al., APL 60, 2204 (1992) .

Basically, all armchair tubes are metallic. One out of three zigzag and chiral tubes show a very small bandgap due to the curvature of the graphene sheet, while all other tubes are semi-conducting with a bandgap that scales approximately with the inverse of the tube radius. Bandgaps of $0.4 - 1$ eV can be expected for SWNTs (corresponding to diameters between 0.6 and 1.6 nm) [10].

One of the most exciting aspects of carbon nanotubes is their tremendous potential for applications. They exhibit very interesting mechanical properties [11].; similarly to the graphene from which they can be considered as derivatives, carbon nanotubes are among the hardest materials known today [11] and are particularly resistant to deformation parallel to the main axis of the nanotube. Young's modulus of multiwall is approximately 800 GPa, close to the calculated value for the in-plane modulus of graphite, 1.06 TPa [11].

Carbon nanotubes are also ideal candidates for novel molecular devices since their electronic properties depend both on their geometry and on doping by impurities; by controlling these parameters it is possible to realize carbon-based electronic devices [12].

Another important field of application of carbon nanotubes is the emission field effect; Fink et al. [13] recently developed a low energy electron projection microscope where the electrons are extracted by applying a voltage between the sample and a MWNT emitter. The nanotube provided a highly coherent beam that allowed the acquisition of in-line electron holograms of the observed objects with a quality comparable to atom-sized W emitters.

Other devices could be fabricated by taking part of junctions between a metallic and a semi-conducting tube. Such a junction would behave essentially like a Schottky barrier, which is widely used in semiconductor devices. A large number of theoretical and experimental hurdles have to be overcome before such nanoscale devices will be realized. But in principle, by combining different nanotubes and sublementing these with gate electrodes, a large variety of electronic components ranging from wires, bipolar devices to field-effect transistors could be embodied.

Another important field of applications of nanotubes are biotechnologies [14]; in fact it is possibile to decorate the outer surface of nanotubes with biological macromolecules, to promote

the development of new biosensors and bioelectronic nanomaterials. Such devices could take advantage of the specific biomolecular recognition properties associated with the bound macromolecules.

One step in that direction has been realized by Balavoine et al. [15], who successfully crystallized the protein streptavidin on the outer surface of a carbon nanotubes.

1.2 Carbon nanowires

Linear carbon chains (or carbon nanowires) are a monodimensional allotrope of carbon, where the carbon atoms have a sp hybridization state [16]. These structure have a general formula C_nH_2, with n>4 (see Fig. 10). Carbon atoms are connected each other by alterned triple and single bonds; this structure is in equilibrium with the polycumulenic form, where all the carbon atoms are connected by double bonds (Fig. 6).

$H\text{-}C{\equiv}C\text{-}C{\equiv}C\text{-}C{\equiv}C\text{-}H$ $\qquad$ $H_2{=}C{=}C{=}C{=}C{=}C{=}H_2$

(a) (b)

Fig. 5: The polyynic (a) and cumulenic (b) forms of linear carbon chains.

The cumulenic isomer has a higher content of free energy and is therefore more unstable than polyynes [17] .

Chains are usually terminated by H atoms, but in some cases, on depending by the solvent used for their production, they can be terminated by CN groups [18].

The formation of carbon nanowires is a competitive process with respect to the formation of fullerenes and nanotubes; in certain operating conditions the formation of sp2 species becomes unfavourite and sp-hybridized carbon chains are formed.

It has recently demonstrated the possibility to insert these structures inside a single-wall nanotube, through a process called nanotubes unzipping, in order to obtain a nanocomposite material composed by a nanowire inserted inside a nanotubes.

This kind of interaction stabilizes the nanowire chain, that would be otherwise quite unstable.

1.3 Highly Oriented Pyrolitic Graphite

Highly Oriented Pyrolitic Graphite (HOPG), as it is well known, is a sp^2 carbon-based material, which is composed of superimposed graphene layers joined together in a lamellar structure by van der Waals forces.

As it is well known, a graphene layer is composed by C atoms with sp^2 hybridization with a 120° angle between two interatomic bonds, so that in a virtually pure HOPG system only sp^2 hybridized C atoms are present [19]. For this reason, HOPG is commonly used as a typical reference system when pure sp^2 signals are needed.

This system is strongly anisotropic from a structural point of view; actually, if we consider the basal surface of a 001 graphite, we have a well ordered plane of C atoms sp^2 hybridized superimposed one-another; on the other hand, when we consider the edge surface, then we face a structure where only the C atoms in the borderline of each plane are visible [19].
Due to the distance between the planes that matches the wavelength of X-rays, HOPG graphite can be used as a monochromator for this radiation.

1.4 Graphene

Graphene is a two-dimensional sheet of sp^2 carbon atoms, a layer of carbon atoms arranged in condensed hexagonal rings [20]. Graphene is a unique macromolecule for its flat, bidimensional structure and one of the strongest materials ever studied. Its charge carriers exhibit giant intrinsic mobility, have zero effective mass, and can travel for micrometers without scattering at room temperature. Graphene can sustain current densities six orders of magnitude higher than that of copper, shows incredible thermal conductivity and stiffness and it is impermeable to gases [21]. It is certainly a candidate material for nanoelectronics and nanocomposites. Additionally, a surprising reactivity of graphene has been demonstrated since, quite unexpectedly, graphene is able

to react with hydrogen forming graphane regions in a graphene sheet [22].

This discovery may have consequences in astrochemistry research in relation to the mechanism of molecular hydrogen formation in space and in modern technology either for applications both in the creation of insulator ‘‘lands’’ in highly conductive graphene sheet or for hydrogen storage systems [23,24].

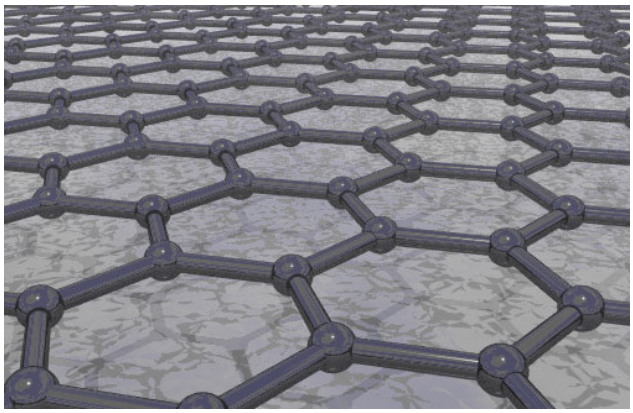

Fig. 6: A grapheme sheet, with sp2 hybridized carbon atoms.

Graphene is one of the most resistant nanomaterials that are known, the Young's modulus relative to the stretching along an axis lying on the floor is equal to 0.5 Pa, about half that of graphite [25]. As recently demonstrated, a sufficiently large 2D structure, in the absence of applied lateral tension, will bend and crumple to form a fluctuating 3D structure [26]. Ripples have been observed in suspended layers of graphene, and it has been proposed that the ripples are caused by thermal fluctuations in the material; in this sense it is debatable if graphene is a truly 2D structure.

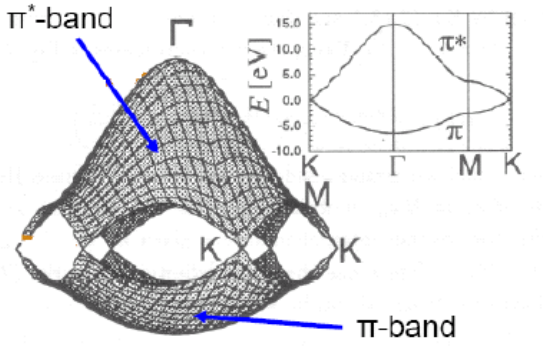

Fig. 7: A scheme of electronic structure of graphene, together with its relation of dispersion.

Due to its particular electronic structure, graphene exhibits a very high opacity for an atomic monolayer (about 2.3 % of white light is absorbed).

1.5 Inorganic nanowires

There is a growing interest in these last years in the production and the characterization of inorganic nanowires and a growing group of researchers in the nanotechnology community study inorganic rods, tubes, and related nanoscale structures. The area of inorganic nanowires is of great scientific and technological interest because by synthesizing semiconductor (e.g. Si, GaN, etc.), dielectric (e.g. SiO_2), or metallic (e.g. Ni, Pt) nanowires, the level of functionality in future nanosystems may be greatly enhanced. It is now possible to also synthesize stoichiometrically complex oxides, nitride, and carbides that exhibit exotic properties.

Such additions to the series of available 1D nanomaterials may open opportunities for novel devices and applications.

To date devices and components such as field effect transistors, decoders, inverters, UV sensors, LEDs, lasers, chemical sensors, and biosensors based on inorganic nanowires have been tested and are in some cases in production. Both the synthesis of such nanostructures and their integration into larger scale systems are today a field of great interest to the research community for the huge impact on the technologies fields.

In particular, MoSI nanowires (see Fig. 9) are composed by Mo6 octahedral clusters joined together through sulphur bridges; each Mo atom is bound to I atoms [27].

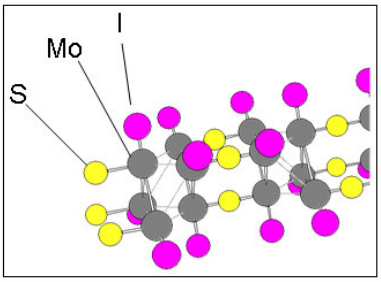

Fig. 8: Structure of the $Mo_6S_3I_6$ nanowire.

These systems are very easy to be dispersed and purified in the most common organic solvents; moreover, they exhibit intriguing mechanical and electrical properties, with a nearly metallic conducibility which is independent on their particular stoichiometry [28,29]. Due to these properties, MoSI nanowires are emerging today as one of the most interesting objects in the field of materials science and are studied for many applications, like bionsensors and chemisensors, field emission effects, composites

and molecular-scale connectors in molecular electronics. One of the most common of these systems, $Mo_6S_{9-x}I_x$ presents a structure of Mo6 octahedral building blocks bridged by S atoms that lie at the centre of the wire; each Mo atom is terminated by I atoms on the outside of the wire.

These structures are conductive and all have identical electronic properties; importantly, they can be easily dispersed in common solvents, down to individual nanowires [30].

These materials are therefore possible candidates to a wide-scale usage for the realization of electronic nanocircuits; in these structures MoSI nanowires act as a connectrors, while metal particles, as gold, silver or mercury, act as nodes [31].

Together with inorganic nanowires, also inorganic nanostructures Mo-S based, i.e. MoS_2, are studied today for their intriguing properties. These compounds exhibit a layered structure very similar to that of graphite. In details, molybdenum sheets in bulk MoS_2 are sandwiched between two sulphur ones, with the metal covalently bounded to six sulphur atoms in a trigonal pyramidal coordination mode. These layers are held together and stacked along the c-direction by van der Waals forces. The weakness of these bonds confers very low friction coefficients, giving unique mechanical properties frequently used in lubrication applied to metallic and ceramic surfaces, in environments where hydrocarbons or other fluid-based lubricants are unsuitable, such as in high vacuum or high temperature. Moreover the semiconductive nature of molybdenum sulphides (band gap ~ 1.78 eV) also allows a wide range of applications in nanoelectronic and in photovoltaic processes since it well matches the solar spectrum.

1.6 MoS_2 fullerene-like nanostructures

A significant number of sulfides and, more generally, transition metal chalcogenides exhibits a lamellar structure. These materials consist of layers within which the atoms are covalently bonded, while atomss belonging to different strata interact through weak van der Waals forces.

This structural feature determining the existence of some properties shared by most systems in layers, like the tendency of the material to flake according to directions parallel to the basal planes and the ability to host atoms or molecules in the interplanar space. The stoichiometry of the chalcogenide layer is a type of MS_2. Unlike graphite, whose layers have a thickness of monoatomic, dichalcogenides in each molecular layer are composed of three atomic layers, arranged in the sequence S / M / S ("sandwich" structure).

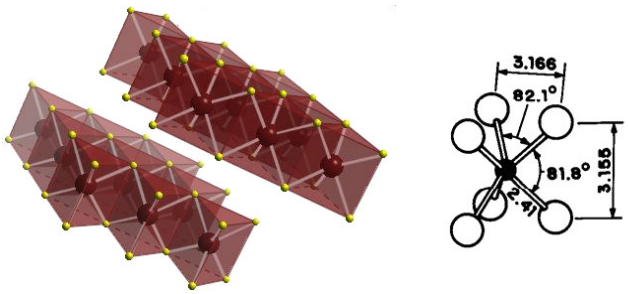

Fig. 9 : Layer structure of molybdenite (MoS_2).

These compounds (hereafter referred to as LTMC, layerd dichalcogenide transition metal) exhibit very interesting physical and chemical properties, which can also be modified by intercalation or reduced in the form of nanostructures. In particular, the molybdenum disulfide (MoS_2) is a material widely used in various application fields such as catalysis, tribology, conversion and energy storage. In fact it is widely used as a catalyst in the hydrodesulfurization process (HDS) and other processes. Although such use is well established for several decades, still the research aiming to understand the reaction mechanisms, and then to 'optimization of catalytic processes, is extremely active. The molybdenum disulfide is used, alone or as an additive for lubrication of mechanical parts subjected to high loads, high temperatures and / or vacuum conditions. In this context, there is considerable interest both for the development of techniques for the deposition of antifriction coatings of MoS2 in the synthesis of nanostructures that can be used as additives for lubricating oils for high performance.

The intercalation of alkali metals between the layers of MoS_2 or other LTMC is a property of particular interest, both from a purely scientific point of view and for possible technological applications. Attention is directed towards the interlayer lithium, for the potential of MoS_2 as the cathode in rechargeable lithium batteries. Furthermore, the properties related to the electronic structure of MoS_2 make it a material of interest for the construction of solar photovoltaic panels.

The following sections describe in more detail the physical properties of molybdenum disulfide, discussing the similarities and differences with other LTMC.

Later we will discuss the properties and procedures for synthesis of nanostructures based on molybdenum disulphide and similar compounds.

Chapter 2 .Experimental Section

In this part of the thesis I describe the experimental work carried out on different classes of nanomaterials described above. In order to study in details the properties of 1-D systems, we felt it necessary to make even a preliminary study on structures that may be regarded as the forerunners of such systems, in particular graphite and graphene.

We then continued the study of carbon nanostructures-based 1-D, poliini and carbon nanotubes in terms of production and characterization methods with innovative methods of spectroscopy and microscopy.

The one-dimensional overview of the systems could not be considered complete without including those in our study may include some of the most interesting discoveries in the field of nanostructures, both in terms of production and functionalization, both in terms of characterization.

2.1 Carbon-based nanomaterials

2.1.1 XPS characterization of edge and basal planes of Highly oriented pyrolitic graphite

As we previously discussed, graphite can be considered as the result of stacking each other many graphene layers, bound together

by the weak van der Waals forces. HOPG is one of the most studied carbon materials.

As is well known, a graphene layer is composed of C atoms with sp^2 hybridization with a 120° angle between two interatomic bonds, so that in a virtually pure HOPG system only sp^2 hybridized C atoms are present.

For this reason, HOPG is commonly used as a typical reference system when pure sp^2 signals are needed.

This system is strongly anisotropic from a structural point of view; actually, if we consider the basal surface of a 001 graphite, we have a well ordered plane of C atoms sp^2 hybridized superimposed one-another; on the other hand, when we consider the edge surface, then we face a structure where only the C atoms in the borderline of each plane are visible.

Despite its apparent simplicity, HOPG presents XPS features that are still far from being fully understood. A very controversial point in even very recent literature is, for example, the origin of the typical asymmetric shape of the C1s signal. HOPG only has one single type of interatomic bond, which is the C-C bond sp^2 hybridized so, basing on this evidence, one would expect a very sharp and symmetric peak at a binding energy (BE) value corresponding to the sp^2 system; on the contrary, the C1s peak shows an asymmetric shape with a tail towards the higher binding energy values.

A lot of works are present in literature, from the ‘70ies to nowadays, aimed to justify this peculiar shape and to obtain an univocal and complete description of the complex processes involved in the interaction X rays-electrons in such a system and,

therefore, in the C1s signal shape. One of the first model was proposed in 1979 by van Attekum and Wertheim [32]; they found a peak shape characterized by a singularity index of 0.14 and explained this observed asymmetry with the formation of excitonic final states close to the Fermi level, which are responsible of the tail observed at higher binding energy. Sette et al. [33] confirmed that the line asymmetry is similar to that associated with metallic screening related to the excitonic states formation, but found a smaller singularity index (0.05-0.1) respect to the first work.

Yang and Sacher [34] claimed that the C1s peak of a totally defect-free graphite is symmetric and that the asymmetric shape experimentally found is essentially due to the presence of surface defects.

Another common model was proposed for the first time by Balasubramanian et al. [35], who argued that the C1s peak of HOPG can be fitted by two components, due to a surface and bulk contributions, separated by 0.12 eV. Similar argumentations were made by Takata et al. [36] and Smith et al. [37], who arrived to similar conclusions of Balasubramanian et al., but found different values of singularity index.

This intense debate lasts until nowadays with an article of the end of 2008 by Hunt [38], who again proposes the two-components model already described, but also demonstrates that the surface and bulk contributes are associated with the higher and the lower binding energy components respectively.

As already mentioned, edge and basal surfaces are completely different from a structural point of view and is therefore reasonable to expect a different behaviour in terms of electronic structures and

of XPS signals as a consequence. Moreover, on the basis of a work by Larsson et al. [39], who made an ab initio study of the energetics involved in the nucleation process of diamond in HOPG substrates from the vapour phase, we know that the surface free energy of the C atoms on the edge surface is higher than on the basal surface; in fact the authors demonstrated, in agreement with a previous paper by Chen and Yang [40], that the reactivity of C atoms toward the adsorption of atomic hydrogen to form sp^3 bonds increases going from the basal face to the armchair face and to the zigzag face of the edge atoms, which have therefore the highest tendency to react, due to the thermodynamic instability of the C atoms in that structural configuration.

The stability of the basal surface is also confirmed by Ooi et al. [41] who claims that this surface undergoes no noticeable relaxation and no reconstruction as the strong covalent bonding prevents any corrugation modification of the basal planes. On the other hand, for what above discussed, it is reasonable to expect a possible surface reconstruction where the C atoms of the edge surface rearrange themselves in a more stable configuration.

XPS study made on a HOPG sample by analyzing the two surfaces above described, i.e. edge and basal, and by studying their C1s, VB and Auger spectra. The VB analysis, in particular, is of a great importance because it allows to studying the density of states close to the Fermi level which is a sort of “fingerprint” of a specific atomic structure.

The obtained results evidence, as expected, great differences between the two surfaces; while for the basal surface we obtain a

confirmation of a sp^2 hybridized structure, with a C 1s peak shape similar to those present in literature, the results we obtain for the edge show a surface where the sp^3 hybridized structures are present in a very large extent and are strongly preponderant respect to the sp^2 domains, that are however still present.

The edge surface has also been analyzed after a thermal treatment at 600 °C in order to test its stability; the result is a further rearrangement of the structure leading to a pure sp^2 system, similar to that of the basal surface, due to the thermally-induced rearrangement of the borderline atoms.

In Fig. 10 the spectrum obtained on the HOPG basal surface (blue line) is reported.

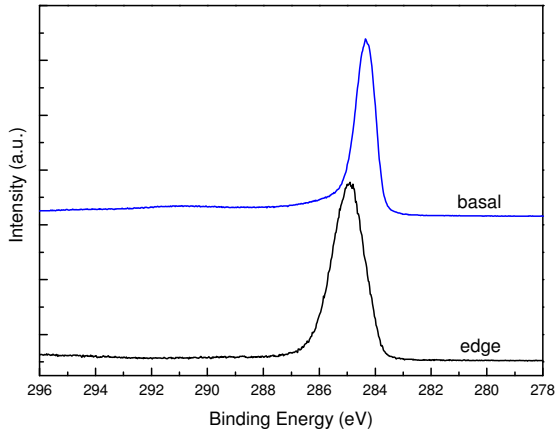

Fig. 10: C 1s spectra of the basal and edge surfaces. It is evident the asymmetric shape of the first spectrum, while the edge one is quiet symmetric. The chemical shift of 0.7 eV about is also evident.

The C1s peak is found at a binding energy of 284.3 eV, which is the typical value expected for a pure sp^2 system [42]; the spectrum

clearly shows an asymmetric shape, with a tail towards the higher binding energy values. This result is widely expected and, as above discussed, has been the subject of an intense scientific debate.

A totally different situation is found when analyzing the edge surface; infact, when looking at the black line in Fig. 1, we find a C1s signal at a BE of 285.0 eV, which is a typical value of a sp^3 system [43]. Another important evidence that comes out from the comparison of the two spectra is that the typical peak asymmetry of the sp^2-basal system has now disappeared and the C1s spectrum of the edge surface is symmetric, as expected for the C1s spectrum of a sp^3 species [44].

We also find the same C1s shape spectrum in other two points of the edge surface, analyzed in order to have a good statistics of the its surface chemistry.

The distance between the three points analyzed was ~ 2mm, which is a much greater value with respect to the X-ray spot size (700 * 400 μm).

The analysis of the VB spectra strongly corroborates these conclusions; consolidated literature data [45,46] identify three main ranges in the VB of carbon materials: signals between 7-8 eV are assigned to pure p orbitals, those around 10-15 eV to hybridized s and p orbitals and peaks in the range 17-20 eV to pure s orbitals. In our case, as shown in Fig. 11, we find for the basal surface (blue line) a wide maximum centered at 18-20 eV about, a first pronounced shoulder at 14 eV and a second weak shoulder at 8 eV. These data are typical of a sp^2 hybridized C system [47] and, therefore, there is a perfect correspondence between the information obtained from C1s peak and that obtained from the VB

study. The data so far described are therefore related to a nearly defect-free sp^2 surface, which is the one of the basal HOPG. Fig. 11 also shows three VB spectra (edge I, edge II, edge III) taken, on the same three points, in order to obtain a good statistics of the chemical composition of the edge structure.

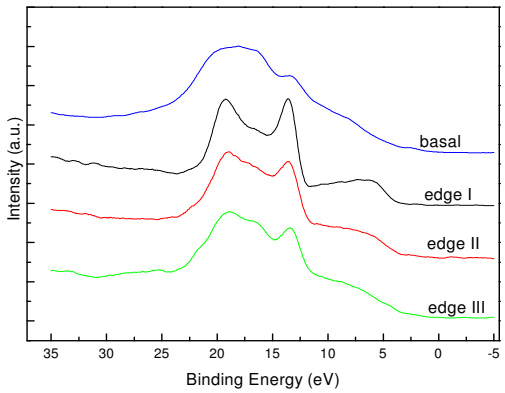

Fig. 11 X-ray excited VB spectra taken on a point of the basal surface and on three different points of the edge surface. The basal spectrum is representative of a pure sp^2 system while the edge I strictly reflects the spectra of pure sp^3 systems reported in literature. The other two edge signals can be considered as intermediate between the sp^2 and sp^3 spectra.

From the examination of this Figure, we note a strong similarity between the three VB spectra obtained on the edge and the spectra of sp^3 systems like diamond or polyethylene [48,49], thus suggesting that we are analyzing a nearly pure sp^3 system on the edge surface. Actually, from literature data we know that the VB line of pure diamond or polyethylene are constituted by two distinct peaks at 19.3 and at 13.5 eV (sp^3 signal), and by a shoulder at around 7.5 eV, that are the same values we find in our spectra. In particular, the edge I spectrum is very similar to the polyethylene VB, while the other two spectra present a strong similarity with the

diamond VB. Therefore, these experimental results reveal a complex edge structure, that is mainly constituted by sp^3 systems and where both diamond-like carbon and polyethylene moieties are present.

It also should be noted that the edge II and edge III spectra could be considered as intermediate between the VB of pure sp^3 system and the VB of the pure sp^2 basal system. Indeed, even if these spectra present the same maxima and the same BE values of sp^3 systems, we note that the peak at 13.5 eV has a lower intensity and the band at 19.3 is broader similarly to what we find in the VB of a sp^2 system.

The same results can be obtained if we consider the C KLL Auger spectra of the basal and edge surfaces, reported in Fig.12, in which X-ray excited Auger spectra taken on the same points of the C1s and VB spectra are shown; the spectrum of the edge III point is not reported since it is very similar to the edge II one.

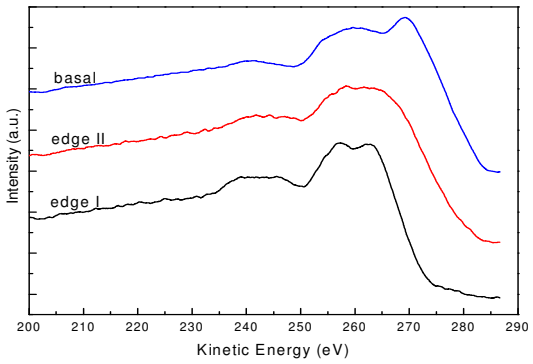

Fig. 12. X-ray excited Auger spectra taken on the same points of the VB spectra (the edge III spectrum is not reported as it is identical to the edge II). The situation of edge II and edge III can be considered as intermediate between basal and edge I, showing an inhomogeneous surface composition.

The analysis of the figure shows, again, deep differences between the basal, where sp^2 systems are preponderant, and the edge surfaces, where sp^3 structures are mainly present. Once again, edge II can be considered as an intermediate situation between the pure sp^2 and sp^3 systems represented by the basal and edge I spectra respectively. These conclusions are in agreement with literature data that demonstrate the possibility not only to discriminate between graphite, diamond and diamond-like carbon through the analysis of the X-ray excited Auger spectra [50] but also to evaluate the corresponding sp^2:sp^3 ratio.

Therefore, these data describe a rather inhomogeneous surface chemical composition on the edge, where we find a strong preponderance of sp^3 system, as evidenced by the VB spectra and the C 1s signal. Nevertheless sp^2 domains are still present, even if in a small extent, as we can realize by the study of the VB spectra (edge II and edge III) that, as already mentioned, show features that are intermediate between the VB of a sp^3 and that of a sp^2 system.

These results can be easily understood remembering that the edge atoms in the graphene planes are in a situation of thermodynamic instability because the sudden interruption of the D6h symmetry of the graphitic plane should leave, under a theoretical point of view, an edge surface with dangling bonds; since it is well known that such kind of bonds can not be present in a real system, due to their high energy content, the system must rearrange its surface structure. The data shown demonstrate that the system reaches this target by changing the carbon hybridization state from sp^2 to sp^3.

In the light of this model, the heterogeneous chemical surface composition of the edge surface can be easily explained, because the bond rearrangement process of the edge atoms is not uniform; sp^3 domains are created during this process and become predominant on the edge surface, but sp^2 structures are still present. Hence changing the carbon hybridization state from sp^2 to sp^3 is the main mechanism used by the system to lower the surface energy; more or less small sp^2 rich domains are still present along the edge surface and, probably, their planar geometry might be distorted.

The lack of homogeneity of the edge is also clearly visible at macroscopic level. Fig. 13 shows a picture taken by optical microscope of the edge surface; as can be seen, the edge surface is macroscopically defective, and it shows large "domains" clearly visible.

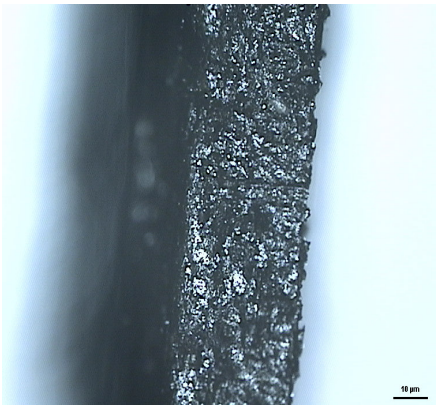

Fig.13: Optical microscope image taken on the edge surface. A macroscopic inhomogeneity of the surface is clearly visible.

This macroscopic heterogeneity is an additional demonstration of what we proved by the XPS data i.e., again, that the edge surface

has a complex structure and, in particular, that domains with different hybridization states are present.

In order to test the thermal stability of the edge surface we heated our sample at high temperature (600 °C for 1 h) under vacuum in the XPS prep-chamber (P~10^{-7} torr) and then we analyzed it again. During the heating ramp, we noted a pressure rising (to about 10^{-5} torr) of a few seconds at the temperature of 350 °C.

Fig. 14 and 15 report, respectively, the comparison preheating-postheating of the C1s peaks and the VB spectra taken on the edge surface.

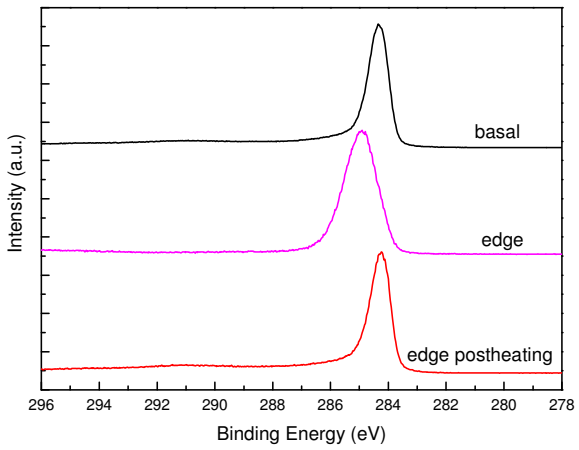

Fig. 14: C1s spectra of the edge surface before (purple) and after (red) annealing at 600 °C. The C1s spectrum taken on the basal surface (black) is reported for comparison. It is evident that the inhomogeneous edge surface, where mainly sp^3 domains are present, is converted in a sp^2 structure after annealing.

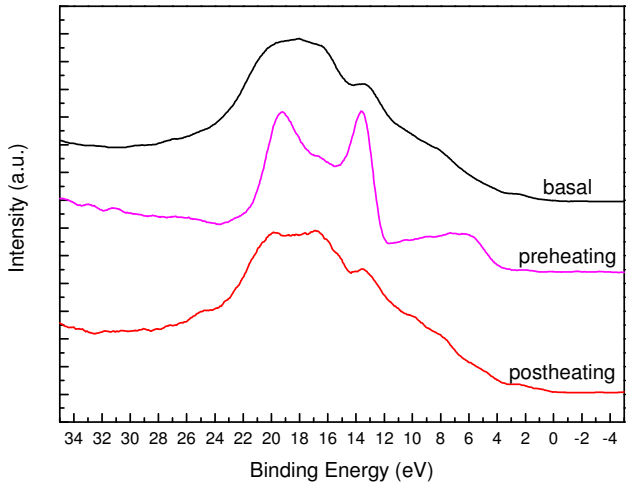

Fig. 15. VB spectra of the edge surface before (purple) and after (red) annealing at 600°C. The VB spectrum taken on the basal surface (black) is reported for comparison.

The analysis of the figure allows to reach same conclusions already discussed for the C1s spectra comparison, i.e. that the edge surface after annealing is converted in a structure where mainly sp^2 systems are present.

It is clearly seen that the C_{1s} peak post annealing has now a BE value typical of a sp^2 system (284.4 eV) and the typical asymmetric shape we already widely discussed for sp^2 C hybrids. The same trend is seen when we take into account the VB spectra; the VB after annealing has the typical shape of a pure sp^2 system, i.e. a broad maximum between 18-20 eV, a first shoulder at 14 eV and a second weak shoulder at 8 eV. The surface analyzed after annealing is now clearly a sp^2 surface.

The high temperature gives energy enough to our system to rearrange to a sp^2 hybrid; a very important result, that must be

underlined here, is that the C1s after annealing presents the same asymmetric shape that we already assigned to the presence of a bulk and two more external components on the basis of the literature data above discussed.

This result clearly demonstrates that, as a consequence of the annealing we observe a structural rearrangement of the edge surface, leading to the formation of sp^2 hybrids that become preponderant over the sp^3. We propose that the only one way in which sp^2 bonding can be present on the edge is the formation of sp^2 domains, that could be viewed as an "extension" of the sp^2 layers of the basal surface, covering the edge surface that remains topographically rough. In other words, the edge surface is now covered by sp^2 domains that are roughly orthogonal to the basal plane.

These results allow to conclude that the edge surface, which has the complex chemical and structural organization above described, is yet susceptible to react to form a further more stable system and, after annealing process, it rearranges in a sp^2 structure which has the most stable configuration under those conditions.

A second possibility, which can not be completely excluded, is that the edge of the graphite surface is contaminated with carbon impurities that depart during the heating under vacuum. In fact, some organic substances such as polyethylene to give a typical signal of the sp^3 carbon at 285 eV that can be confused with the signals that could be formed by restructuring sp^3 carbon atoms terminals.

In order to have a confirmation of the restructuring took place in the edge area, we have analyzed a new piece of graphite.

In this case, we have analyzed the surface after a thermal treatment at 600 °C under vacuum in order to verify the presence of organic contaminants that must evaporate in those conditions. We heated the sample in the XPS pre-chamber by subjecting it to a heating time of 1 hour at 600 ° C. After warming up we retested the sample that no longer showed sp^3 signals. During the warming a degassing happened which led to an increase in the pressure value in the prechamber, as evidenced in Fig. first chamber, described by Figure 16.

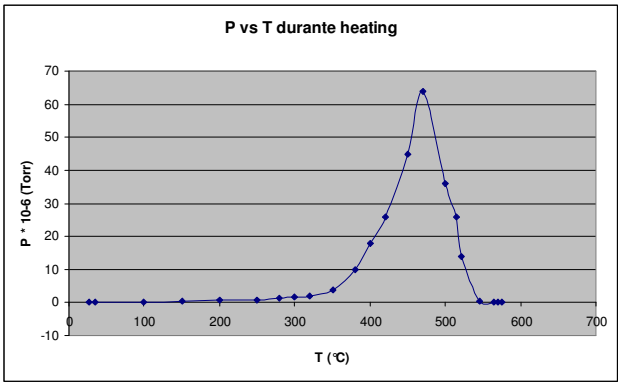

Fig. 16: Increase of the pressure value in prechamber during the heating ramp, due to degassing of organic contaminants. The phenomenon lasted for about five minutes, then pressure reached its usual value (~10^{-8} Torr).

This indicates that, after heating, the sample of graphite releases a gaseous chemical species; the increase of pressure observed in the pre-chamber is maintained for about 5 minutes, after which the pressure has back to the normal values insured by the turbo pump (range of about 10^{-8} Torr).

The sample has been subsequently analyzed showing no sp^3 signals. We then exposed the graphite sample to atmosphere for a week, after which we proceeded to a new analysis. The surface edge of the sample so treated, after a week of exposure to air, showed no signals attributable to sp^3 structures, indicating that the surface undergoes no spontaneous restructuring, at least in the range of exposure to the air that we considered. The presence of sp^3 structures, found in the initial analysis of the surface edge, could be therefore attributed to the presence of organic surface contaminants (e.g. polyethylene, etc ...).

2.1.2 Synthesis of Graphene form unzipping of carbon nanotubes

As already previously discussed, graphene is a unique molecule for its mechanical and electronic properties, which made him an ideal candidate for applications in nanoelectyronics. In this context, the possibility to develop new and simple synthetic routes to graphene which may be easily expanded on industrial scale, is of a straightforward importance. Numerous works already focused on this specific topic ranging from chemical reduction of exfoliated graphite oxide to the vacuum graphitization of silicon carbide or to the growth of graphene on metal substrates [51-57]. Some of these synthetic procedures to graphene showed already promising potential for industrial application [58]. Recently, it has been reported about the oxidative unzipping of multiwall carbon nanotubes (MWCNT) forming nanoribbons up to 4 lm long with widths of 100–500 nm and thicknesses of 1–30 graphene layers [59,60]. This part of my thesis describes the XPS study of the

products obtained by the oxidative unzipping of single-wall carbon nanotubes (SWCNTs).

Synthesis of carbon nanoribbons/graphene from SWCNT

The graphene from single-wall carbon nanotubes sample was prepared using a method described in literature [62,63] and recently improved [64].

The general synthetic procedure for the preparation of the carbon nanoribbons samples involved the dispersion of 200 mg of the pristine SWCNT in 200 ml of a mixture of concentrated HNO3/H2SO4 in a 1:3 volume ratio followed by 8 h of ultrasonic treatment performed at 50W at 45 °C. To reach neutrality, they were washed with distilled water and finally dried in an oven at 100 °C.

Vibrational analysis

Raman spectroscopy has been used to distinguish graphite from a single or multiple layers of graphene sheets [65]. In particular, the G' band known also as 2D band in graphite is located at about 2700 cm_1 and consists of two components the 2D1 and 2D2 [64]. In a single graphene layer the 2D band appears as a sharp peak located at lower frequency than the 2D2 peak of graphite. Additionally the graphite G band at 1580 cm_1 appears shifted at higher frequencies in a single graphene layer [65]. Fig. 17 shows a comparison of the Raman spectra taken on a HOPG (highly oriented pyrolytic graphite) on a MWCNT and the spectra of the nanoribbons prepared by the oxidative attack of a SWCNT.

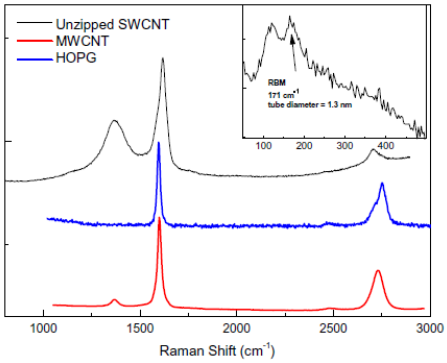

Fig. 17: Raman spectrum of unzipped SWCNT (Carbolex) after oxidative treatment (top trace), higly oriented pyrolitic graphite (HOPG) (middle trace); MWCNT (bottom trace)

Although weak, the 2D band of the nanoribbons appears shifted at lower frequency than graphite and simultaneously the G band appears shifted at higher frequency in comparison to graphite. In Fig. 18 are reported the Raman spectra of pristine SWCNT in comparison to the derivatives nanoribbons.

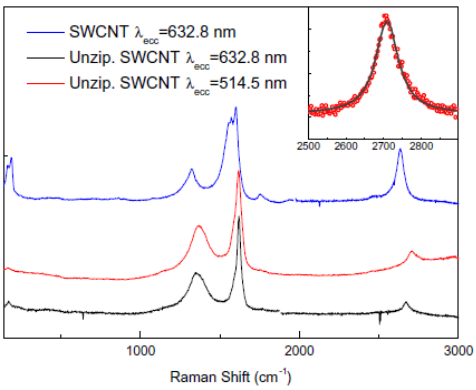

Fig.18: Raman spectra of pristine SWCNT (top spectrum at 632.8 nm excitation) in comparison to the nanoribbons prepared from oxidative cleavage of SWCNT (middle and bottom spectra respectively at 632.8 and 514.5 nm excitation). In the inset is reported the 2D band of the graphene nanoribbons; the band is symmetric and can be fitted by a single Lorentian curve.

The RBM mode of the pristine SWCNT is intense and clearly evident below 200 cm^{-1} but become extremely weak on the oxidized derivatives suggesting that the oxidative cleavage of the SWCNT was successful. From the overall Raman data reported in Fig. 18, a number of intriguing considerations can be done. First of all we observe that the 2D band, measured after the oxidation, appears completely symmetric and can be fitted by a single Lorentian curve (see inset). This could be an indication that the nanoribbons are in some way isolated and not stacked.

Moreover, a careful analysis of the D and G modes reveals that the I_D/I_G intensity ratio increases up to 0.68 (633 nm excitation) after the oxidation and shows a typical dependence from the laser wavelength with a value around 1.04 when the spectrum is recorded using the 514 nm radiation. Similar considerations can be done about the position of the D band, whose origin can be ascribed either to the presence of defects in the nanoribbons and/or to the intrinsic defects given by the plane edges [66,67]

Fig. 19 shows the FT-IR spectrum of the nanoribbons prepared by the oxidative cleavage of the SWCNT.

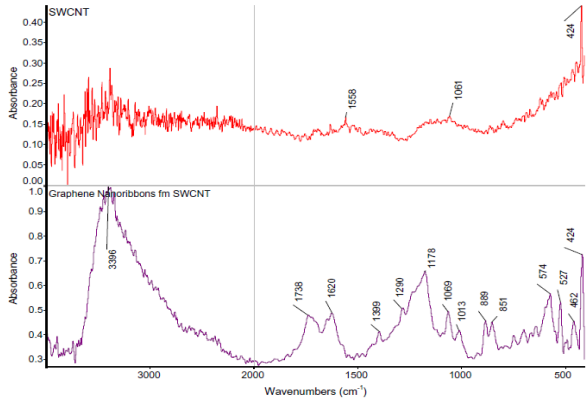

Fig. 19: FT-IR spectra (KBr) of pristine SWCNT (top) and nanoribbons from oxidative cleavage of SWCNT (bottom).

The analysis of the spectrum, as evidenced by the presence of the band in 3396 cm-1, indicates the formation of highly oxidized species and rich in chemical oxygenated groups. In particular, the FT-IR spectrum of the nanoribbons from SWCNT appears quite similar to that of graphite oxide. The -OH groups are suggested by the band at 3396 cm^{-1} by the C-OH bend at 1290– 1178 cm^{-1}, the C-O-C moiety at 1070–1013 cm^{-1} while the presence of ketone groups are indicated by the absorption bands at 1740 and 1620 cm^{-1}. The band at 1740 cm_1 suggests a ketone group in carboxylic acid anhydride and/or in aldehyde, while the 1625 cm_1 feature is typical of a,b-unsaturated ketones [68]. Also epoxyde group is thought to be present in graphite oxide and its presence in the FT-IR spectrum is suggested by the peaks at 889 and 851 cm_1 due to antisymmetric and symmetric epoxy ring deformation [68]. The spectrum of Fig. 4 resembles that of graphite oxide and those of oxidized fullerenes prepared by exhaustive ozonization of C60 or C70 [68].

These data corroborate what has already been observed Raman analysis. Because in fact oxides can be Considered as defects in the nanoribbon structure, this evidence justifies the enlargement of the D-band in the samples after treatment, as discussed during the description of the Raman spectra.

XPS analysis of the nanoribbons obtained from SWCNT

In order to clarify the types of chemical modifications have occurred in our systems as a result of oxidative treatment, we performed XPS analysis. The C1s photoelectron signal is shown in Fig. 20 and it has been deconvoluted into three species.

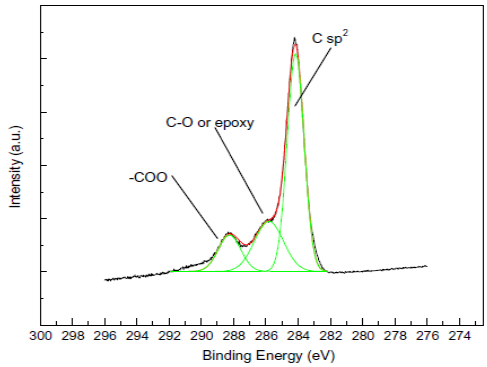

Fig. 20: XPS spectrum of C1s photoelectron signal on nanoribbons from SWCNT. The deconvolution of the spectrum evidences the assignments.

The main peak at about 284.5 eV is due to sp2 hybridized C bond of graphite network (this is the only signal we got on pristine SWCNT samples) while signals a 286.5 eV e 289.0 eV are indicative of the presence of oxygenated species linked to carbon

atoms and are respectively attributed to C-OH groups or epoxy groups and carboxylic groups [69].

The formation of oxygenated species linked to carbon atoms is easily attribuibile al trattamento ossidante effettuato con HNO_3 e H_2SO_4. Similarly, the signals of the S_{2p} and the N_{1s} show the presence of oxygen species;

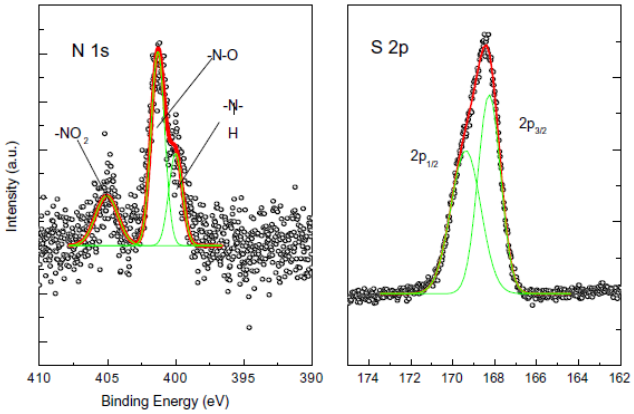

Fig. 21: XPS spectrum of N1s and S2p (a) photoelectron signal on nanoribbons from SWCNT. The deconvolution of the spectrum evidences oxygenated nitrogen and sulphur species present in the sample.

in particular, sulphur signals are located at 168.2 and 169.1 eV and attributable to both sulfonic (-SO3H) and sulfate (-OSO3H) or other oxidized sulphur species [70] chemically bound on the graphene nanoribbons. On the contrary, nitrogen shows photoelectron signals at 400.0, 401.8 and 405 eV, thus suggesting the presence of nitro groups and nitric acid bound to graphene surface [71].

TEM analysis on the graphene nanoribbons obtained from SWCNT

The effect of oxidative treatment on carbon nanotubes was also studied by TEM. Figure 22 shows the comparison between the TEM images of nanotubes before and after oxidative treatment.

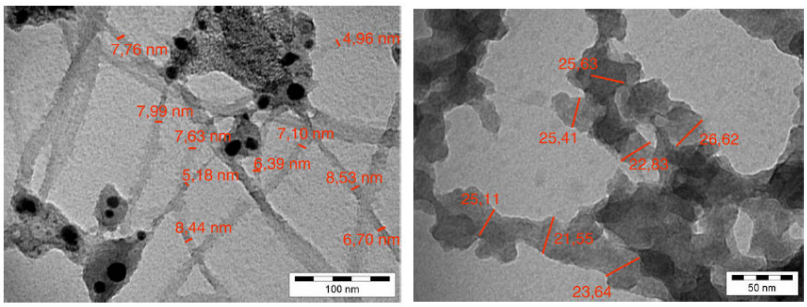

(a) *(b)*

Fig. 22 Comparison between the TEM images of the samples before (a) and after (b) the oxidative treatment.

As it is evident, there is a strong modification of samples, in particular, observe the thin sheet of graphene (nanoribbons) have an average width of about 22-26 nm. These structures may show tendency to stack together into overlapped layers although in many areas of the TEM image (Fig. 22) also appear single sheets.

It is important to highlight that, as evidenced by the the average size of the nanoribbons, these can be considered as derivatives by the opening of a single nanotube.

The TEM image also shows larger areas, which show that the nanoribbons obtained by the opening of the nanotubes in some cases give rise to phenomena of aggregation and overlap with the growth of lateral dimensions and height of the aggregates. The study carried out by TEM allows then to corroborate what has

been observed through spectroscopic analysis, namely that carbon nanotubes are completely open as a result of treatment with oxidizing acids and lead to the formation of graphene nanoribbons fairly homogeneous in size.

AFM analysis on the graphene nanoribbons obtained from SWCNT

In order to measure the height of the aggregates of nanoribbons obtained as a result of oxidative treatment, thereby identifying the extent of the phenomena of aggregation and overlap, AFM analysis was performed on the samples after treatment. The AFM analysis shows a very complex and varied in the size and type of structures formed as a result of treatment. In particular, the AFM image shown in Figure 23 shows that approximately 10% of the surface is covered with aggregates with typical lateral dimensions from a couple of 100 nm up to several micrometers.

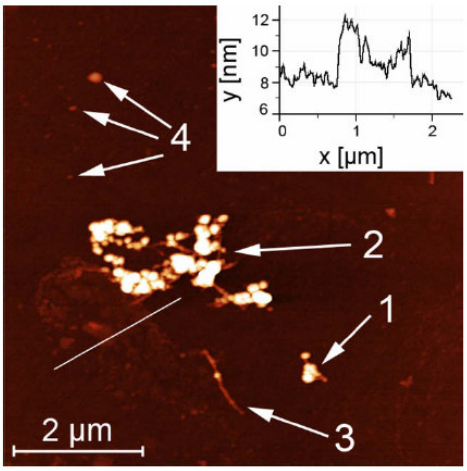

Fig. 23: AFM topography image (5 · 5 lm) of the graphene nanoribbons sample. The inset in shows the profile taken across the line indicated in the lower-left corner of the image.

The maximum height of these aggregates ranges from 100 to 200 nm. Together with this kind of macroaggregates we also observe the presence of island-like structures (arrow 4 in Fig. 23) whose typical height and diameter fall in the range of a few to several tens of nanometers. Another type of structure (arrow 3 in Fig. 23), resembling a tube, can be found on the sample surface with a typical height and width of 10 and 200 nm, respectively. In fact, a careful analysis, it is possible to note that the macroaggregate shown by the arrow 2 is a mixture of island-like structures and tube-like structures.

The rms roughness across the sample may vary as much as an order of magnitude (as seen in many AFM images – from 3.75 to 0.32 nm). No areas with a smaller amount of material could be found on the surface (i.e. one cannot observe only the substrate surface).

Additional features appearing to be some kind of trenches or steps are also observed in the topographic image. It is not clear whether these are features of the substrate or this is also graphene, because no areas without graphene could be found on the surface.

These trenches/ steps measure a few A° in depth/height (up to _6 A°). Figs. 24 (a) and (b) show the height and effective diameter distributions of islands, respectively.

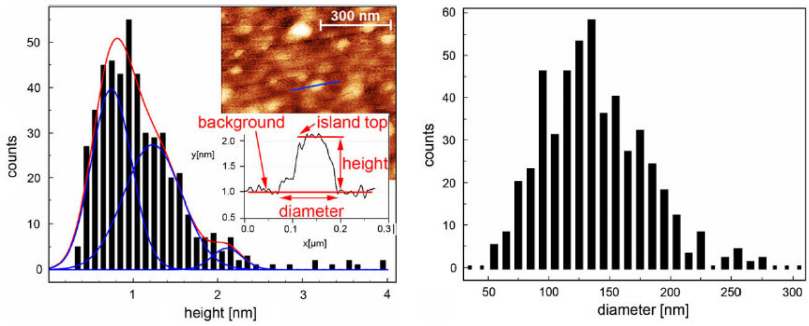

(a) *(b)*

Fig. 24: (a)Nanoribbons islands height distribution measured with AFM. Solid lines represent a fit of a sum of three Gaussian distribution to the experimental data (in red color the sum of the two blue Gaussian). (b) Effective nanoribbons island diameter distribution. The average island diameter is 136 nm.

In Fig. 24(a) solid lines represent a fit of a sum of three Gaussian distributions to the experimental data (purple color – individual gaussian distributions, light blue color – sum of the three Gaussian distributions). The inset in Fig. 24(a) shows an AFM image and a height profile of an island from which the island height and effective diameter were determined. The actual diameter of the island is smaller than depicted in the inset of Fig. 24, because the island shape in the image is a convolution of the tip shape and the actual island shape; however, for islands with heights (1–2 nm) much smaller than the tip radius (10 nm or more), this only results in an absolute shift of the effective diameter distribution towards larger values. The height of the islands was determined as the height difference between the island ‘‘top’’ and the ‘‘background’’, as can be seen in the inset of Fig. 24(a).

The average height of the islands is 1.17 nm while the average roughness on top of these islands was measured to be _1.7A°. Although there are no sharp peaks in the island height distribution, the shape of the histogram in Fig. 24(a) suggests that there is more

than one ‘‘group’’ of islands present on the surface (i.e. the islands may consist of one or more layers). Three Gaussian distributions were used to fit the data shown in Fig. 24(a). If one takes into account only the positions of the three peaks (0.74, 1.22, 2.11 nm), one can calculate the thickness of a single ‘‘layer’’ of graphene: d = (0.70 ± 0.20) nm.

Fig. 24(b) shows the effective diameter distribution of the same group of islands: an average island diameter of 136 nm is obtained. By plotting the effective island diameter against the island height, it appears that there is some correlation of the island height and the island diameter. In fact, a linear fit y = A*x + B was used (x being the island diameter and y being the island height) and the following values were obtained for the fit parameters: A = 9.27.10_3, B = _0.114.

2.1.3 Carbon nanotubes produced by arc discharge in liquid nitrogen

Since the discovery of fullerene, carbon materials with reduced dimensionality have been considered among the most interesting systems in materials science because of their large implication in nanotechnology. In particular, carbon nanotubes (CNTs) and other one-dimensional carbon systems are considered very promising for their appealing mechanical, optical and electronic properties. Many CNTs synthesis methods are based on the ignition of hot carbon plasmas [72,73], such as in the case of the laser ablation of carbon

targets or in the case of arc discharge processes between two graphite electrodes.

These experiments are generally carried out in vacuum or inert atmospheres, while only a limited number of studies have been reported in liquid environments [74]. Despite this, the use of a liquid as an environment during the process has the advantage to avoid any vacuum system, leading to a cheaper production way and gives the possibility to study the effect of different chemical species on the growth process. Moreover the analysis of the liquid after the plasma ignition is interesting since the trapped species can be easily analyzed and simply correlated to specific, active components during the nanocarbons formation. In this part of my thesis, by using both laser ablation and arc discharge approaches, I analyze, compare and discuss the species formed during the plasma ignition and trapped in the liquid phase (liquid nitrogen), correlating them with some features of the nanostructures (mainly carbon nanotubes) formed at the cathode during the arcing procedures.

The ablation of graphite targets has been conducted in water (Millipore grade) and CH_3CN (Analytical grade) using pulses (5 nsec, 532 nm) of a Nd:YAG laser. The irradiation has been performed at room temperature, the optimized laser energy density was found to be around 1 J/cm2 and the irradiation time was set at 20 min. Regarding the arc discharge setup, we supplied a voltage (25 V) to two graphite rods (electrodes) immersed in liquid nitrogen, setting the current at values up to 80 A. Different experiments have been performed by using (cylindrically shaped) anodes and cathodes with diameters in the range between 5 and 10

mm. The structural characterization of the samples was performed by scanning electron microscopy (SEM) and transmission electron microscopy (TEM), while untreated and unfiltered liquids have been analyzed immediately after the processes by performing UV extinction spectra in the range 200-500 nm.

Raman spectra have been excited by the 514.5 nm radiation from an Ar ion laser and the scattered light has been confocally collected and analyzed by a Jobin–Yvon 450mm monochromator equipped with a CCD detector cooled at 77 K. In the case of the linear carbon chains (polyynes) found in the liquid phase, the Raman spectra have been taken after the deposition of some drops of liquid onto a silver surface suitable for Surface Enhanced Raman Spectroscopy [75,76].

Analysis of the residue after the plasma ignition

Fig.1 compares the UV absorption spectra of the residual species found in the liquid immediately after the ignition of carbon plasmas by the ablation of a graphite target in water or acetonitrile and by arcing between two graphite electrodes in liquid nitrogen (after Cataldo [77]). All the spectra are representative of the absoption of polyynes. These intriguing molecules with alternating single and triple bonds (general formula C_nH_2) are considered precursors for the formation of nanotubes and fullerenes [78] and possess 'per se' intriguing nonlinear optical properties [79] as well as a π-electron system suitable for the application in nanoelectronics for conductance switching and negative differential resistance at single molecule levels [80].

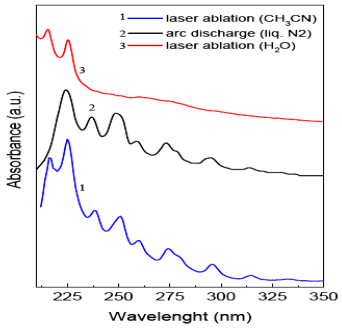

Fig. 25. Comparison between the UV absorption spectra (a) of the residual species found in the liquid immediately after the ignition of carbon plasmas by the ablation of a graphite target in water or acetonitrile and by arcing between two graphite electrodes in liquid nitrogen.

Coming back to the absorption spectra reported in fig.25, it is interesting to observe that while in the case of the ablation in water the spectrum is very simple and provides two signals located at 215 and 225 nm (belonging to C_8H_2 species), the absorption data found for the ablation in CH_3CN and for the discharge in liquid nitrogen is much more rich. Moreover the spectral pattern in these two last cases indicates that the species formed and trapped in the liquid are the same: the structures located between 220 nm and 340 nm are indicative of the presence of polyynes with a length up to $C_{16}H_2$. After laser ablation or arc discharge processes at low or moderate currents (below 20 A) some carbon material is either suspended in the liquid or slightly deposited on the targets (electrodes).

Deposition and analysis of carbon nanostructures at the cathode during arc discharge

When the arc discharge experiment is conducted at moderate or high current values (above 20 A) a short time (10 s – 30 s) is sufficient to get a considerable carbonaceous deposit at the cathode. As an example, Fig.26 (a) shows a SEM image of the deposit after arcing between two graphite electrodes in liquid nitrogen: it appears a sponge-like surface containing a great amount of thin nanotubes, as evidenced in the higher magnification image shown in Fig.26 (b). At a macroscopic scale, the deposits have size and shape which mimic the anode geometry.

Moreover other experimental evidences indicate that the growth rate of the nanotubes is related to the geometry of the setup as well as to the specific discharge conditions [81].

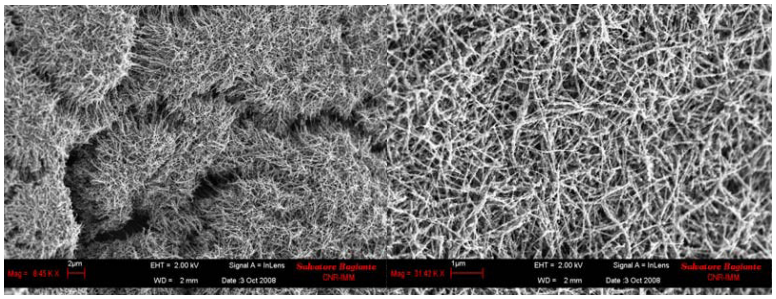

(a) *(b)*

Fig.26. SEM image of the deposit after arcing between two graphite electrodes in liquid nitrogen at low (a) and high (b) magnifications.

Even though literature presents a large number of experiments in which the arc discharge method is used, a direct correlation between discharge parameters (current, voltage, electrode geometry) and the properties of the carbon deposit is hard to be achieved because of several differences in the various approaches.

In order to gain information on a specific set of experiments and correlate them to the properties of the nanotube grown, we report in fig.27(a) some Raman spectra for the carbon deposits as a function of the discharge current. The spectra are taken on samples produced by using electrodes with a 6 mm diameter. In each spectrum typical D and G signals appears at around 1360 and 1580 cm^{-1} respectively. As widely known the intensity ratio (I_D/I_G) between these two signals is an indication of the structural order of the carbon structure [82-84]. Fig.27(b) also reports the I_D/I_G values as a function of the discharge current, for different electrode diameters (anode/cathode: 5mm/6mm, 6mm/6mm, 10mm/10mm) and definitely confirms that the quality of the produced nanotubes as well as the materials growth rate are strictly correlated either to the current and to the electrode geometry.

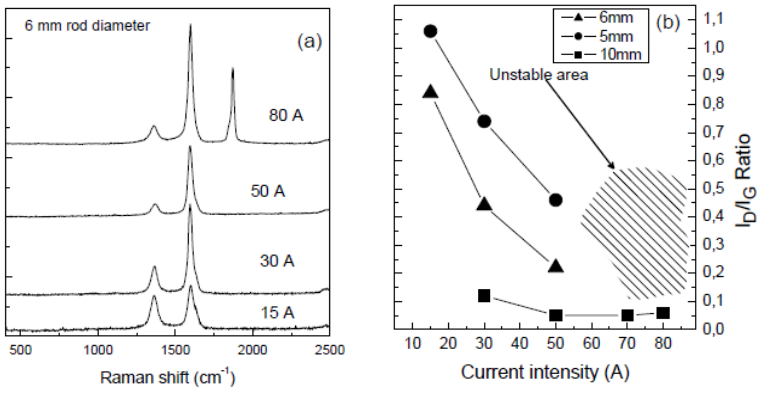

(a) *(b)*

Fig.27: Raman spectra (a) of different deposits obtained at different currents with a 6 mm electrode configuration. In particular the spectrum at 80 A is obtained with unstable arc discharge conditions. The I_D/I_G integrated ratios are reported in pat (b) as a function of the discharge current.

The behaviour quantitatively described in fig.27 can be interpreted on the base of the Gamaly model [85] for the nanotube growth.

Following this approach, the CNT formation in an electric discharge is driven by the ratio between two velocity distributions (anisotropic and isotropic or Maxwellian) for the C+ species formed in the plasma. The anisotropic distribution is due to the strong potential drop, at around 12 μm far from the cathode surface, which accelerates the C+ ions towards the cathode itself, while the isotropic one is related to the carbon atoms/ions expelled from the cathode surface for thermal effect. It is supposed that the formation of carbon nanotubes and other carbon nanostructures occurs when these two groups of ions impact. The anisotropic travelling species are then involved in building up a nanotube in length, while Maxwellian carbons are responsible for the nanotube growth in width. At high current values the first group predominates and, consequently, we get the formation of longer low-defective nanotubes, while at low currents it is outnumbered by the isotropic species, leading to shorter and more disordered products (like the carbon onions, horns or beanpod structures), that contribute to the increase in the I_D/I_G ratio.

The same fig.27 (b) reports a discharge instability region, observed at high discharge current values (70 A- 80 A) in the case of both anode and cathode with 6 mm diameter. In such conditions, Raman spectra performed in different regions of a carbon deposit show very different I_D/I_G ratios, therefore having a nearly complete lack of homogeneity. Nothing similar is found for the samples produced with the 10 mm rods, where the I_D/I_G values are very low and do not even show any considerable variation for different discharge current values. We argue that, if a sudden current interruption occurs, like in the case of an unstable arc, the anisotropic

component immediately disappears and the isotropic velocity distribution dominates the process. From the spectroscopic point of view, carbon deposits produced under unstable discharge conditions reveal additional Raman signals like those reported in fig.27(a) (80 A) at around 1850 cm-1. Raman features in this spectral range generally belong to sp-hybridized carbon systems [86] thus confirming the presence of polyynes in the solid deposit. It has been recently argued that such linear carbon chains can be arranged into the inner walls of the carbon nanotube [87]. Some of them have been also directly observed by TEM (see fig.5), evidencing a peculiar bottle-neck shape for the inner CNTs.

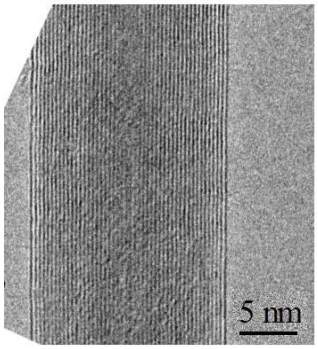

Fig.28. Linear carbon chains inserted into a MWCNT observed by TEM. Its is also evident a peculiar bottleneck shape for the inner CNTs at the end of the chain.

The micrograph shows also that the diameter of the innermost tube suddenly changes from 0.9 to 0.7 when the linear carbon chain appears (see arrow in fig.5). This means that the distance between the linear chain and the nanotube inner wall is just the typical distance between two graphene sheets, in agreement with the

findings by Zhao et al. The data are also confirmed by the study of the radial breathing modes as reported elsewhere [88].

Comparison of the observed carbon nanonanostructures

The experimental findings discussed up to now suggest that during the discharge a complex series of reactions between carbon radicals and ions (mainly C_2 and C_2^+) produce a variety of sp-hybridized carbon molecules [89]. Some of them remain trapped in the liquid environment, while other contribute to the formation of the carbon nanostructures if a suitable driving force (the electric field in the case of a discharge) is able to collect them, for instance at the cathode.

Moreover, we have already discussed that in a laser ablation experiments, we never observe the formation of carbon nanotubes, while a plenty of nanowires (polyynes) are obtained. We noticed the same result in arc discharge experiments with currents below 20 A. From these considerations, it is our opinion that the formation of nanotubes is related either to the possible formation of long linear carbon chains and to the presence of a (strong enough) driving force which leads these chains to interact each other, as in the case of arc discharge experiments at high currents. In the case of the nanotube formation at the electrode, if the growth process is not completed or it is frequently interrupted (like in the case in which strong current instabilities are present), some carbon nanowires can remain trapped inside the nanotube, thus forming the observed nanotube-nanowire hybrids. We have already shown that Raman spectroscopy readily indicates the occurrence of the presence of sphybridized carbon systems.

For this reason we compare in Fig.29 the spectra as taken in the carbon deposit and in the collected liquid residue.

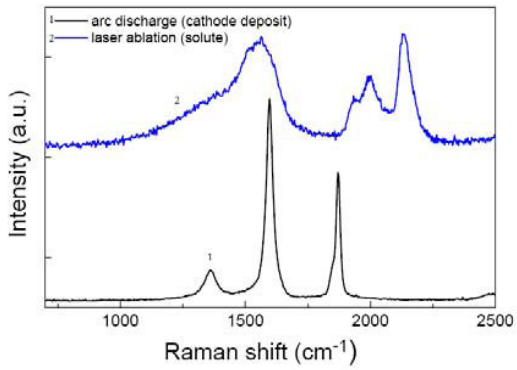

Fig.29 Comparison between the Raman spectra of the deposit collected onto the cathode (in the case of the formation of the hybrids) and the material left into the liquid after an ablation process.

Apart from the differences observed in the D and G line region due to different graphitization processes, we observe that the nanowires inserted into the nanotubes have stretching signals which are strongly red shifted with respect to free polyynes. This can be understood considering that the position of the -C≡C- stretching is inversely proportional to the chain length [90] and that the chains inserted into the nanotubes are certainly much longer than 20 carbon atoms. Furthermore it has been recently observed that a moderate contribution to the red shift could come from an interaction between the linear carbon chain and the nanotube walls which soften the carbon bonds [91]. Finally it has been observed that carbon nanowires inserted into the nanotubes are much more stable with respect to free linear chains. Then the understanding and the control of the formation processes can be useful for specific

applications of these 1D carbon materials with intriguing properties.

2.1.4 Interaction Nanowires-Noble metals

Surface Enhanced Raman Scattering (SERS), is a spectroscopic technique in which a supporting roughened metallic surface acts as an amplifier for the Raman intensity of chemical species adsorbed on this surface [92]. The SERS effect, that is receiving a renewed attention in the last few years especially in the field of sensor chemistry and trace analysis, is still an argument of intense debate among spectroscopists since the true nature of the phenomenon is yet not clear in a complete way [93]. In particular the long scientific diatribe started thirty years ago between the chemical (charge transfer) or electromagnetic (local field) nature for the Raman intensity enhancement seems to be still actual. Probably an equal mixture of both effects is the true reason for the intensity enhancement, even if the prevalence of one effect on the other depends on the specific interaction surface-adsorbate and on the nature of the adsorbed chemical species. In this frame the use of surface protecting species as for instance SAM, may give a rough indication on the importance of the electromagnetic effect because when long chain alkane-thioles are adsorbed on a SERS active surface the modulation of such an effect results a function of the alkanethiol length [94]. Linear carbon chains (or Carbon NanoWires, CNWs) containing sp hybridization, either as alternating triple and single bonds (polyynes) or with consecutive

double bonds (polycumulenes), are interesting molecular structures because they represent the building blocks and precursors often used to form fullerenes and carbon nanotubes. These systems, as well as other novel carbon allotropes such as graphene or graphyne, have been synthesized and characterized using a variety of different methods [95-98]. Most of these experiments have revealed the extreme instability of the produced 1D carbon structures with respect to chain-chain cross linking reactions and exposure to oxygen which generally lead to a reorganization towards more stable sp^2 phases. In the last two years a considerable effort has been done in the investigation of linear carbon chains through the use of SERS [99]. Indeed this technique couple the powerfulness of Raman spectroscopy to characterize the hybridization state of carbon atoms and the possibility to detect small amount of materials through the interaction (electromagnetic or chemical) of the molecules onto suitable metallic surfaces. The enhancement cross section in SERS can be attributed to the excitation of a surface plasmon resonance in metal nanoparticles as well as to local mixing of molecular and metal energy levels leading to a phenomenon similar, under certain limits, to that occurring in the resonance Raman effect. Another interesting reason to explore the CNW-metal interaction is given by the possibility to use CNWs in the field of nanoelectronics. Indeed has been recently argued that these conjugated oligomers are very promising in conductance switching and negative differential resistance at single molecule level [100]. A direct bond with metallic surfaces is then very appealing as well as the study of the interaction between these carbon nanowires and suitable metallic surfaces. Since the works

by Tabata et al. [97], silver nanoparticles suspensions and/or roughtened silver surfaces have always been used to generate the SER effect, confirming that the interaction of polyynes molecules with silver happens by substitution of hydrogen capping atoms with the metal cation. Differences in the spectral features found using the SERS techniques with respect to Normal Raman (NR) have been attributed to these interactions. Lucotti et al. [101] have shown that for polyynes produced by electric arch discharge between two graphite electrodes submerged in liquid environments, the C_8H_2 specie has always been found to be the dominant one, and that the two broad bands evidenced by SERS analysis cannot be reproduced by DFT calculations on Ag terminated polyynes. These should be justified either with the presence of cumulenic linear chains, or with the dimerization of C_8H_2 (to form $C_{16}H_2$) assisted by the metallic surface catalytic effect.

In this respect we would like to point out that the induced polymerization of many monomer/oligomer onto nanostructured silver surfaces has been observed though SERS spectroscopy [102]. In these cases, it has been revealed that the process is partially photon assisted during the measurement execution. Since up to now enhanced Raman spectroscopy on polyynes has been essentially conducted using silver in the form of nanoparticles assemblies or roughened surfaces, we conducted a series of experiments devoted to the investigation of the interaction between these molecules and other metallic surfaces capable to give SER effect. Moreover the use of differently prepared metallic nanostructures have been employed in a set of experiments with the aim to better highlight differences and similarities. Thus nanometric spacers have been

also used in some cases to avoid a direct contact with the metallic surfaces, giving further insight for the presently discussed polyyne-noble metal interactions.

Experimental Section

Polyyne solutions were prepared by laser ablation of solid graphite targets in water and hexane as described elsewhere.17. Millipore grade water (5 ml) and n-hexane (HPLC grade) have been used and the ablation has been induced by using the second harmonic (532 nm) of a pulsed Nd:YAG laser (Continuum Surelite II, 5 nsec pulse duration, 10 Hz repetition rate). The irradiation has been performed at room temperature, the optimized laser energy density was found to be around 0.4 J/cm2 and the irradiation time was set at 20 min. This resulted a good compromise between the observation of appreciable spectroscopic signals and the degradation of the polyynes. This process has been in fact observed to increase with increasing the product concentration. The untreated and unfiltered solutions have been analyzed immediately after the ablation by performing UV extinction spectra in the range 200-500 nm to test the presence of polyynes through their characteristic sharp absorption signals.

Laser ablation in water has been also carried out to produce silver and gold colloidal suspensions starting from pure metal targets. The properties of these colloids has been previously investigated through spectroscopic as well as microscopic techniques [103].

One of the major advantages of this method is the formation of reproducible-size controlled colloids, free of chemical contaminations and by-products that are generally obtained using classical chemical metallic salt reductions. In order to obtain suitable SERS surfaces, both gold and silver particles have been deposited onto glass and silicon substrates by deep coating, thus obtaining surfaces uniformly covered with the metal nanoparticles. A microscopic view of a typical silver surface is reported in Figure 30a. The picture has been obtained by AFM microscopy in tapping mode. Some samples have been kept in contact with 1-dodecanethiole (1-DDT), 1-octadecanethiole (1-ODT) or 1-decanethiole (1-DT) solutions (0.1 M in hexane) for 10-24 h in order to incubate the nanoparticles.

After incubation, the SAM solution was removed and copious amounts of hexane where flushed through to remove all the in excess unbounded thiols from the surface. In the same Figure 30 plasmon resonances (PR) for silver and gold colloids are reported. The PR features indicate the formation of nanometersized spherical clusters. We can gain some indication of the polyyne-surface interaction looking at the differences between PR spectra of naked and polyyne covered SERS active surfaces. These differences are shown in Figure 30. As may be seen, whilst for gold (Figure 30b) we do not noticed any difference between bare and polyyne covered surfaces, the PR spectrum of silver (Figure 30c) shows a remarkable red shift. We would like to underline the absence of the typical UV polyyne absorptions. This fact is attributable to the strong inter-band transitions in both noble metals that cover the polyyne UV absorption falling in this same wavelength region.

Once the SERS active surfaces have been obtained starting from gold and silver colloids, the same polyyne solution has been deposited on several SAM protected or naked metallic surfaces, leaving the solvent to evaporate freely at room temperature. Before and after the carbon nanowire deposition, all the samples obtained onto a glass substrate have been analyzed by taking the extinction spectra in the range 200-1000 nm using a Perkin Elmer Lambda 2 spectrometer. Raman spectra have been excited both by the 514.5 nm radiation of an Ar ion laser and the 632.8 nm of a He-Ne one in backscattering geometry. The backscattered light has been analyzed by a Jobin Yvon 450 mm monochromator, equipped with a CCD detector cooled with liquid nitrogen. A macro configuration has been used in order to avoid heating effects of the samples with an estimated laser power density of ca. 1 mW/ cm^2.

Results

A clear indication of the differences, already observed in the PR spectra of Figure 30, between silver and gold surfaces in adsorbing and detecting the carbon nanowires is given in Figure 31.

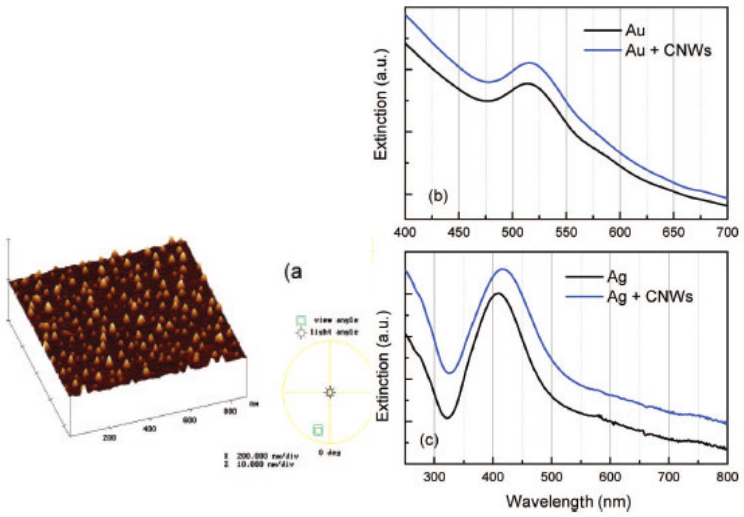

Fig. 30: AFM microscopy of the surface obtained by covering a silicon substrate with silver nanoparticles obtained by laser ablation in water (a). Comparison between PR spectra for naked and polyyne covered SERS active samples in the case of gold (b) and silver (c).

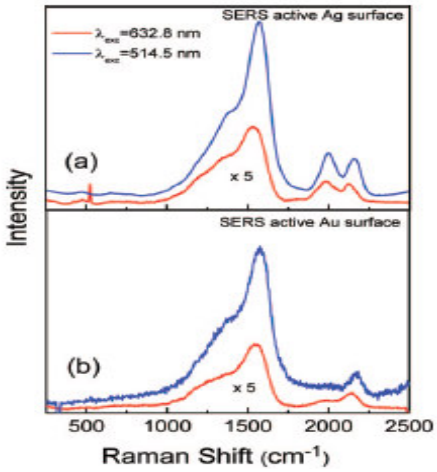

Fig. 31: SER spectra of polyynes adsorbed on silver (a) and gold (b) SERS active surfaces. The samples have been probed using two different exciting wavelengths: 514.5 and 632.8 nm

Here we report SERS spectra relative to the deposition of the same polyyne solution (obtained by ablation of graphite in water) on the

metal nanoparticles covered surfaces. The spectra have been taken using both 514.5 and 632.8 nm exciting radiations, because of the known different SERS magnifications of the two metals expected by using the green or the red line. As usual the spectra are composed by a lower wavenumber region where the sp^2 scattering of amorphous carbons are located. This is extending between 1000 and 1700 cm-1 and is generally composed by a two-band broad signal, characteristic of graphitelike amorphous carbon. As a matter of fact, it is always very difficult to know whether or not this contribution is given by a residual contamination of the metallic surfaces, or by a degradation process of the polyynes before or after the adsorption or also to the presence of other carbon species produced during the ablation of graphite in the liquid. Anyway the most interesting region is the one above 1800 cm-1, extending up to 2250 cm^{-1}. Here sp-hybridized carbon species give their contribution to the scattering.

The position and the intensity of such features depend on the following factors:

(i) the chain length

(ii) the metal-carbon interaction

(iii) the polyynes' capping groups.

As widely reported in literature [104], polyynes obtained by laser ablation or arc discharge in water or hydrocarbons are essentially hydrogen terminated and their length vary between H-(CtC)2-H and H-(CtC)10-H, so the position of the scattering signals can be attributed either to the metal-carbon interaction (compared with normal Raman spectra) or to the carbon nanowire chain length. Nanowires adsorbed onto silver surfaces show two main bands at

2130 and 1980 cm-1 in agreement with several experimental observations and independently from the excited radiation (514.5 or 632.8 nm).

Assignment of these two structures has been firstly attempted by Tabata et al. [97] with a series of NR and SER spectra of size separated polyynes. The SER spectra differ significantly from the NR ones. The bands seen in SERS are generally shifted to lower frequencies compared to those in the NR spectra and are roughly four times broader. Both these effects are due to the molecule-surface interactions that produce a bonding charge transfer at surface level with a lowering of the CC bond order and hence of the relevant stretching frequencies. The significant differences between the SER spectra and the NR ones are thought to arise from the interaction of each polyyne with the Ag islands even though such interaction has not been yet extensively investigated. This observation is in agreement with results given by Pockrand [105] and Manzel [106] where acetylene-silver interaction has been studied. These works account for the downward shift with respect to free acetylene molecule of 40 cm-1 for molecules adsorbed approximately parallel to the silver surface with weak p interactions and 90 cm-1 for those chemisorbed on special Ag sites in a mono-dentate manner.

A minor effect has been observed by a close inspection of fig. 31. Indeed there is a moderate frequency increase of both 2130 and 1980 cm^{-1} modes by increasing the excitation energy. A previous work [107] has shown that free polyyne molecules do not provide any Raman shift by resonance effect, suggesting that this spectral

change can be due to a variation in the electronic configuration of the molecules upon adsorption. This could lead to different resonance processes with respect to those in hydrogen terminated species. The observation that the SER spectra of each adsorbed polyyne give two intense features has been recently discussed by Compagnini et al. experimentally, [108] and by Lucotti et al. theoretically [101]. The first authors observed that the degradation induced spectral changes are not compatible with the assignment of the Ṛ′and _′lines to the same molecular species, while the second researchers pointed out with DFT calculation on Ag substituted polyynes that the strong broad band at low frequency cannot be reproduced by the theory. Such a scenario suggests two explanations for the appearance of the 1980 cm^{-1} feature:

(i) the band is in a frequency range of cumulenic linear chains;

(ii) there is a dimerization of the most abundant species (giving the signal at 2130 cm-1) assisted by the adsorption. This last consideration is consistent with many experimental findings by Cataldo [109] which has observed that a key step for an easy and clean formation of carbynoid structures and polyynes is a Glaser reaction in which a polymerization process takes place as follows

2M-(C ≡̣C)*n*-M+H298

M+

O2

H-(C ≡̣C)2*n*-H (a)

H-(C ≡̣C)*n*-H98

+M+

M-(C ≡̣C)*n*-M+H_2 (b)

or related mechanisms. This has been efficiently proven for copper and silver (M is the metal in the above scheme). We strongly believe that this is the reactive path induced after the chemisorption on SERS active silver surfaces, giving rise to the spectra reported in Fig. 31(a).

Up to now the experiments directed towards the adsorption of carbon nanowires on metallic surfaces, performed either for the stabilization of these structures or for the observation of very low concentrations through the enhanced Raman techniques, has been essentially reported using silver nanostructured surfaces or colloidal clusters. An instructive comparison for the understanding of the CNW-metal interactions and the assignment of the vibrational features is given in Fig. 31(b) where the same polyynes as those adsorbed on silver have been deposited on a gold-nanocluster covered surface. Again the SER spectra have been obtained either using 514.5 and 632.8 nm excitations.

The most intriguing result is the appearance of a single dominant band at 2130 cm^{-1} with a mild, almost negligible structure at lower wavenumbers, suggesting that on gold surfaces the Glaserlike reaction is not so efficient as for silver or it is at least negligible. This fact is not surprising because the reaction requires metallic ions that are more difficult to be obtained in the case of more noble gold metal. One can also wander if it is possible to even partially shield the silver surface to decrease the interaction between the adsorbed molecules and the metallic surface. This must be done with only a mild decrease of the Raman enhancing factor. The use of monolayer protected metallic surfaces through the adsorption of

alkanethiol molecules can be considered a good strategy for the final goal under the given constraints.

Alkanethiol molecules have shown the capability to form a SAM onto noble metal surfaces if adsorbed through a M-S covalent bond [110]. Some Authors have used this strategy to study the surface enhanced Raman mechanism avoiding a direct chemical interaction of any foreign molecular specie with the silver, already covered with the monolayer [94]. It has been also observed that the adsorption of thiols is able to remove carbonaceous impurities with a surface enhanced active sample, because of the strong sulphur-metal affinity [111]. This fact generally reduces the strong intensity differences between Raman signals coming from sp^2 and sp hybridised species in the relevant scattering regions.

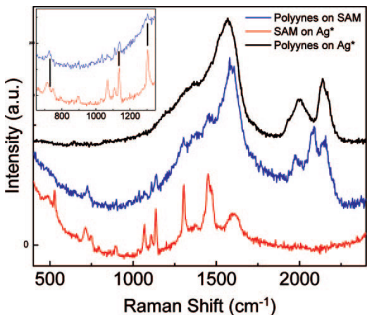

Fig. 32: Three SER spectra revealing the effect of a SAM nanometric spacer. Here we compare SER spectra of carbon nanowires on both a SERS active (Ag) bare silver surface and a ODT protected one. A SER spectrum of 1-ODT is also shown for a comparison. The inset show a detail of the C-S stretching region. All the spectra have been taken using 514.5 nm excitation wavelength.*

Fig. 32 shows a typical SER spectrum of 1-ODT molecules adsorbed on a silver surface composed by the aggregation of silver clusters as those shown in Fig. 29. The chemisorption of the alkyl chain is demonstrated by the absence of the SH stretching signal

which should be present at around 2600 cm^{-1}. The spectrum also shows that only the C-S trans stretching signal is present due to the molecular self assembling, and the absence of any carbonaceous contamination as previously observed. Other relevant features are C-C stretching signals between 1000 and 1150 cm^{-1}, CH2 wagging at 1300 cm-1, CH3 deformations at 1450 cm^{-1}, and the strong CH stretching signals located between 2800 and 3100 cm^{-1}.

Polyyne solutions generated by the ablation of a graphite target in hexane have been deposited on both a bare silver surface and on a 1-ODT protected one. We were forced to use hexane as environmental liquid for the ablation because this liquid is able to wet the CH_3 terminated monolayer thiol surfaces favoring the adsorption. The same Figure 32 compares SER spectra on bare and on 1-ODT protected silver surfaces. Remarkably, in the latter case the sp-hybridized carbon vibrational region presents three definite structures, two of them at the same position as those previously discussed for the polyynes adsorbed on bare silver and another more intense in the middle of these, at around 2080 cm^{-1}.

One of the hypothesis that can be done for the presence of this intermediate CNW feature involves the mechanisms of surface enhancing. The exact mechanism of the enhancement effect of SERS is still a matter of debate in the literature. There are two primary theories and while their mechanisms are substantially different from each other, distinguishing them experimentally has not been straightforward. The electromagnetic theory relies upon the excitation of localized surface plasmons, while the chemical theory rationalizes the effect through the formation of charge-transfer complexes. As mentioned in the introduction, the chemical

effect only applies for species which form a direct bond with the surface, so it clearly cannot explain the observed signal enhancement in all these cases. The enhancement can apply even in those cases where the specimen is only physisorbed to the surface, or it stands at a certain distance from the surface as happens with SAM protected surfaces. In the case of our carbon nanowires we can imagine that a certain type of molecules can diffuse more easily, penetrating between the alkyl chains and thus reaching the silver surface. Here they react forming Ag-(CtC-)*n*H species (2130 cm^{-1} signal) and eventually leading to the formation of dimers (1980 cm^{-1} signal).

This diffusion through an ordered monolayer leaves some structural perturbation which increase disorder and can be seen by a general increase in the linewidth of the C-C and S-C alkanethiol stretching modes. This effect is clearly distinguished in our spectral sequence (see inset in Figure 32). Other polyynes are simply physisorbed onto the SAM surface. For all these last molecules the direct interaction with the metallic surface is inhibited and the enhancement should be given only by the electromagnetic factor. Moreover the position of the C-C stretching should be very close to that observed in a NR experiment. An interpretation of the influence of the chain length, following the existing literature correlation between this chain parameter and the band position, is given in Figure 33.

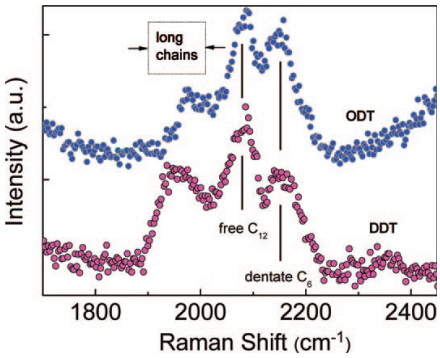

Fig. 33: Detail of the sp-hybridized stretching region in the case of monolayer protected SERS samples after the adsorption of the same polyyne solution. Here two different SAM lengths have been used. All the spectra have been taken using 514.5 nm excitation wavelength.

Here we also compared two different SAM chain length. Accordingly the new 2080 cm^{-1} line increases its intensity by decreasing the molecule-surface distance that is by decreasing the monolayer thickness. Notably, preliminary experiments conducted on gold surfaces do not provide any significant difference with or without a SAM spacer. In order to test the sample stability when polyyne are bound to the noble metal surfaces, we treated some samples with a direct CNW-metal interaction (no SAM shield) with thermal annealings at temperatures up to 150°C. The result are shown in Figure 34.

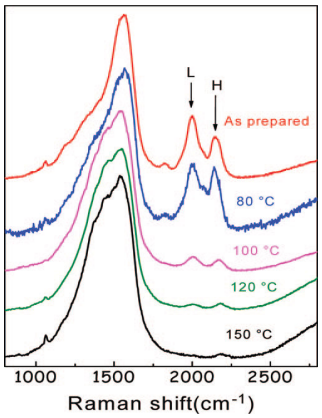

Fig. 34: Effects of thermal treatments for polyynes chemisorbed on bare silver surfaces. L and H refers to long and short polyyne chains, respectively, as suggested in the text.

Two observations deserve to be made owing to these experiments. The first one regards the peaks positions. In fact, while the lower frequency band remains almost unchanged in its frequency value, the higher frequency band increases of almost 40 cm-1 its value. This fact, given in graphic form in the Figure 35, may indicate that the shorter chain polyynes relax their linking with the surface by increasing the temperature, and such a surface bond lowering enforces the triple bond order of the CC conjugated groups.

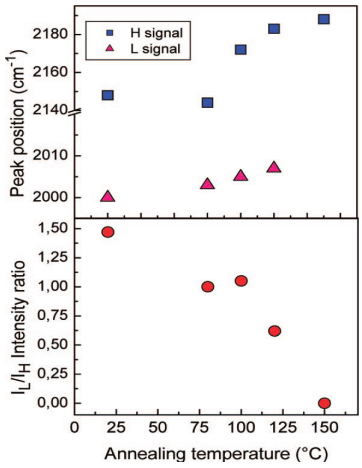

Fig. 35: Position and intensity ratio for the two carbon nanowires signals as a function of the annealing temperature.

The second aspect concerns the persistence under thermal treatment of only the shorter chains on the noble metal surface, being the mode intensity of the longer chains strongly decreasing with temperature increasing. Moreover such an intensity loss for the longer polyynes modes seems to be gained by an intensity increase of the amorphous carbon features in the region 1200-1800 cm-1, indicating an easier amorphization process for the less bonded species and hence a stabilization effect operated by the surface on the better bonded shorter chains. Similar results have been observed by ageing Ag-polyyne colloids at room temperature [112].

2.2 Inorganic nanostructures

2.2.1 Interaction between MoSI nanowires and gold nanoparticles

$Mo_6S_{9-x}I_x$ (MoSI) molecular nanowires have been recently shown to form intriguing large scale self-assembled networks using specific bonding with gold nanoparticles in solution [113,114]. A lot of microscopic studies have been reported in literature, showing the formation of a network between the nanowires and metal nanoparticles, but a definitive study of the bonding states between the two systems is still missing. In order to obtain a clear description of the nature of this interaction, during my Ph.D. work I performed XPS analysis on a nanowires-nanoparticles mixing, together with TEM analyses. The work we made on these systems represents a step forward in the understanding of the structure of these networks through a detailed bonding state analysis. We demonstrate that during the network formation two bonding pathways are observed through the detection of specific Au-S and Au-I bonds. Moreover it is shown that part of the nanowires' integrity is lost after the interaction. Evidences for such behaviour are reported through spectroscopic and microscopic observations using the $Mo_6S_{4.5}I_{4.5}$ stoichiometry.

Besides the bare stoichiometry, the study of the core level signals with their chemical shifts has given the possibility to identify the bonding state of each element constituting the nanostructure. In the present case, such an investigation has been conducted on the

above described systems before and after the interaction with gold nanoparticles.

The gold nanoparticles were prepared by ablation of a bar of gold with a laser having a wavelength of 532 nm for a period of 20 minutes.

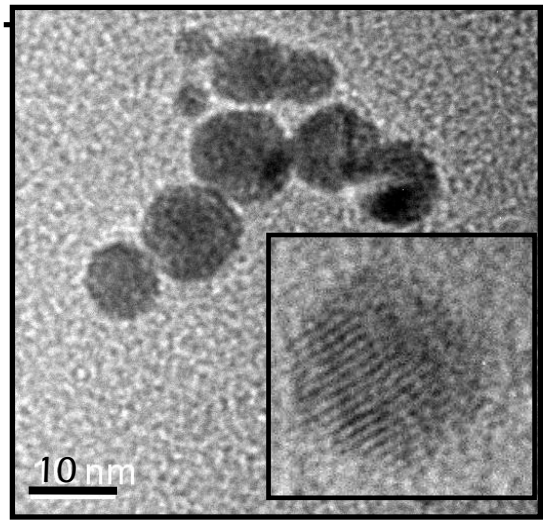

Fig. 36: TEM image of the gold nanoparticles produced by laser ablation in water.

In these conditions we obtain gold particles with a size around 12 nm (Fig. 36). The nanoparticles were mixed with two of MoSI with different stoichiometry:

- $Mo_6S_3I_6$, hereinafter referred to as 636
- $Mo_6S_{4.5}I_{4.5}$, hereafter referred to as 644

The nanowires of the type 636 was dispersed in acetone, while the 644 was dispersed in isopropyl alcohol. In fact, previous studies, it was shown that these nanowires have respectively the maximum

solubility in the two solvents described.

Fig. 37 shows the TEM image of the 644 nanowires produced; we can observe that the nanowires are aggregated into large bundles with a mean diameter of about 18 nm.

This wide bundles can inglobe residual sulphur or impurities as we will see in the following, and therefore we can conclude that IPA does not allow optimal separation of the nanowires 644.

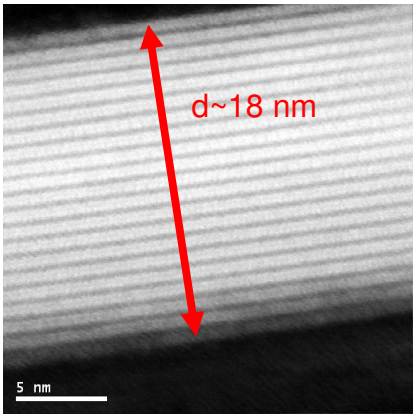

Fig. 37: TEM image of a bundle of 644 nanowires

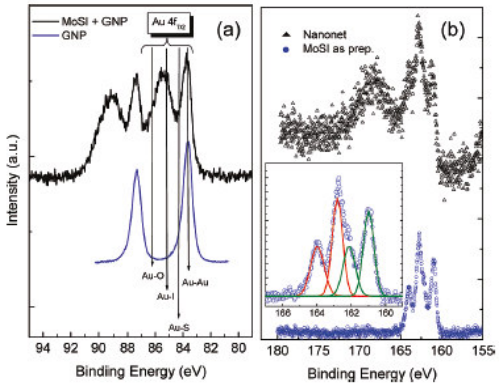

Figure 38: XPS spectra shown in the Au4f (a) and S2p (b) spectral regions. Here we compare the chemical state for these two elements before and after the formation of the GNPs-NW network.

Fig. 38 reports the comparison between the XPS spectra of the gold nanoparticles and of the MoSI nanowires before and after the network formation. The comparison proposed in the figure allows distinguishing strong differences between the signals coming from gold nanoparticles deposited onto a silicon substrate and those coming from the gold atoms at the surface after the interaction with the $Mo_6S_{4.5}I_{4.5}$ wires.

In the first case only two sharp peaks at 83.7 and 87.4 eV assignable to Au 4f7/2 and 4f5/2 respectively are observed.

When interaction between GNPs and MoSI takes place a second doublet is detected at higher binding energies. This highlights an oxidative interaction between the two systems which can be attributed to the bonding of some gold atoms at the clusters surface with either sulphur or iodine belonging to the nanowires structure.

A survey of the available literature was used to attribute [115-117] these components and we report the suggested binding energies in the same Fig.1. Besides the presence of a small fraction of oxidized gold, these results indicate that there is a strong reactivity between MoSI nanowires and gold nanoparticles as already predicted in previous works using AFM and TEM observations [118]. We would like to point out that the nature of the interaction between the metallic nanoparticles and the nanowire's skeleton could not be exclusively due to Au-S bonds, but might also involve iodine atoms constituting the sheath of the nanowire. Moreover, this interaction seems to be quantitatively strong, since at least one half of the Au4f signal is shifted.

In principle, the interaction with sulphur should be detected through an investigation of the sulphur core levels as evidenced in

Fig. 38b, where the XPS spectra for both the “as synthesised” and the Au-nanowires are shown. The two doublets (S2p1/2 and S2p 3/2 see inset in Fig. 38b) shown in the deconvolution can be attributed to the Mo-S bonds occurringin the isolated nanowires as well as to the S-I bonding occurring between the sulphur atoms in the structure of the nanowires and possible residual excess iodine atoms present an interstitial position within the nanowire bundles.

After the interaction with gold nanoparticles, the spectrum presents less clear and intense features (this is probably due to the decrease in the effective number of bundles available on the substrate) and clearly shows signals which are not anymore belonging to sulphur atoms in the original bonding state, as suggested by the broad bump located at around 168 eV in binding energy. It is important to consider that Au-S signals should fall in a region between 161 and 164 eV that is in the same region as for the ‘as synthesised’ samples. Then we cannot exclude that such signals could contribute and overlap to the original MoSI spectral pattern.

Regarding a possible interaction with iodine, TEM images reported in Fig.39 show two typical situations observed throughout the network structure.

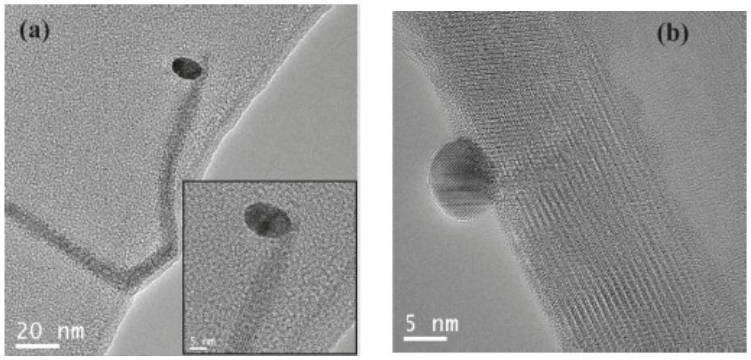

Fig. 39: High resolution TEM images of two typical different bonding configuration after the interaction between gold nanoparticles and a MoSI bundles.

The gold particles appear to be bonded either to the end of the bundles (fig.39a) or to the side of them (fig.39b), allowing an interaction with external iodine atoms to be observed. The reported TEM images are representative of the entire sample and we note a certain discrepancy between the consistent modification of Au4f spectra and the number of particles attached as seen after a microscopic investigation. We could argue that much smaller nanoparticles (clusters with few atoms) might be responsible for a larger modification in the bonding state.

The same interaction is spectroscopically evident in Fig.40a, where the I_{3d} core signals are shown.

In the case of as synthesised MoSI bundles two peaks at binding energies of 620.1 eV and 631.4 eV, corresponding to the iodine 3*d*5/2 and 3*d*3/2 respectively, are recorded. These are due either to S-I and Mo-I bonds in the nanotube structure. In the same spectrum, an additional doublet, accounting the presence of I^-, I_2 and I_2^- coming from residual molecular iodine was also considered. We believe that these impurities can be trapped (stable under

vacuum) in each nanowire bundle. We also found that the larger is the mean bundle size in the sample the higher is the I_2 contribution. After the interaction with gold, we observe a consistent shift of the doublet which reflects an electron enrichment of iodine atoms, related to the interaction with metallic gold, generally considered to be an electron supplier. The signals are also enlarged and present an asymmetric tail towards higher binding energies. Thus we are induced to believe that some nanowires could be partially damaged as a consequence of the network formation. In this respect, note also that the energy of formation for an Au-I bond (average) is lower that that for I-I of about 3.2 kJ/mol and that iodine (ions) have different binding affinity to different gold crystalline facets (adsorb preferentially onto [111] facet [119]).

If damage occurs because of the interaction, this should have consequences in the bonding state of molybdenum atoms too as seen in Fig.40b. Molybdenum has 3*d*5/2 and 3*d*3/2 spin-orbit split contribution. In the case of the $Mo_6S_{4.5}I_{4.5}$ nanowires molybdenum atoms are bonded both with iodine and sulphur and this gives contributions in the range around 228 eV (3*d*5/2) and 230 eV (3*d*3/2). In the case of the as prepared samples this doublet contributes for 87% of the total Mo 3d signal, suggesting that the majority of Mo atoms have the same bonding configuration. Two smaller spin-split Mo *3d* peaks, (13% of the signal) observed at 228.9 eV and 231.9 eV can be attributed to $(Mo_6I_8)I_4$ clusters or to MoO_x impurities ($x \approx 3$).

Once the interaction with GNPs occurs the higher energy component increases in intensity because of the above mentioned

degradation. The relative amount of oxidized molybdenum species are reported in Fig.40c. We readily observe that the interaction of the bundles with gold clusters is responsible for the degradation of a part of the network. This is clear looking at the oxidation of molybdenum and sulphur components (fig.1 and 3) and can be ascribed the exposure to atmospheric oxygen, possibly mediated by a catalytic action of metal nanoparticles, in agreement with the well known catalytic effect of nano-Au on oxidation kinetics [120]. Work is in progress to evaluate the kinetic of this process and to understand the mechanisms.

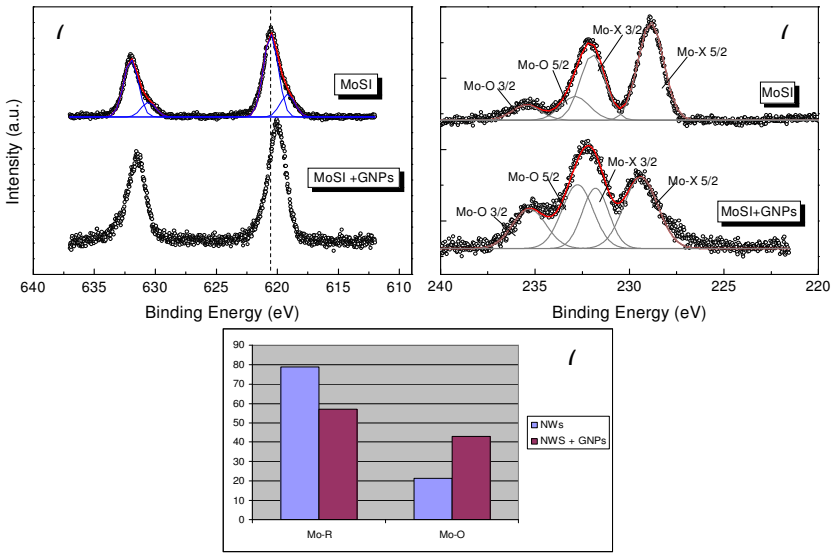

Figure 40: XPS spectra shown in the core I3d (a) and Mo3d (b) spectral regions. This is a comparison before and after the formation of the GNPs-NW network. The histogram (c) shows quantitatively an increased oxidation of the nanowires as a consequence of the interaction.

2.2.2 MoS_2 nanostructures produced by Laser Ablation in Liquid

Extensive research is currently done in order to control the production of inorganic nanomaterials in a proper chemical state and with the desired shapes and dimensions. These studies involve a number of different materials for selected applications such as many nanocrystalline semiconductors and oxides as well as carbon based materials with applications in optics, electronics and catalysis.

From this point of view, pulsed laser ablation of solid targets in liquid environments (PLAL) is emerging as a new strategy to obtain stable suspensions of various nanostructures in a wide range of liquids with a one step-simple and economic procedure. The method is considered a reliable alternative to traditional chemical approaches since such a strategy is considered environmentally friendly ("green" technique) with products which frequently do not need stabilizing molecules or other chemicals. Moreover PLAL is notable also for the low energy consumption required, the absence of any waste by-products and the low loss of material.

Most of the research found in literature is related to the synthesis of metal nanoparticles (including alloys), oxides and carbon based materials leaving enough space for further investigations.

An interesting class of materials is represented by transition metal sulfides with layered structure such as molybdenum disulphide (MoS_2). There has been increasing interest in the synthesis of these sulfides because of their potential applications in areas such as electrochemistry and lubrication, as well as host materials for intercalation chemistry [121] . More recently it has been predicted

and experimentally demonstrated the existence of transition metal chalcogenides nanostructures in the form of fullerene-like (Inorganic fullerene like, IF) nanoparticles, as well as 1D structures such as in the case of MoSI nanowires or bidimensional, atomically thick layers obtained by layer exfoliation of MoS_2, achieved by mechanical processes.

Since most of the synthetic approaches need the use of hazardous compounds such as H_2S and H_2 which are difficult to handle and store [122,123], laser ablation in the liquid phase can be considered as a valid alternative capable to conjugate the gram-scale production of nanomaterials highly stable, under a rigorous control of the process parameters, with environmental sustainability [124].

Herein we show the results of a series of experiments in which MoS_2 targets ha been ablated in water. The target is to obtain IF-MoS_2 nanoparticles and to give a survey of the nanoscale phases obtained through a structural and chemical analysis. This study can be considered as a starting point for further experiments in which other liquids and/or suitable solutions can be used to tailor specific chemical or structural properties for such intriguing nanoscale materials. Our experimental evidences also allow us to propose a growth mechanisms for the MoS_2 nanostructures formation in agreement with theoretical literature data.

TEM analyses

Ablation of MoS_2 in water leads to the formation of a brown colour suspension which is the starting point of our investigation. After filtration, the suspension was drop-casted on TEM supports and analyzed. TEM images, reported in Fig. 41, reveal a large number of structures produced at the nanometric size range. We recognize at least two of them labelled with the letters A and B in Fig. 41a.

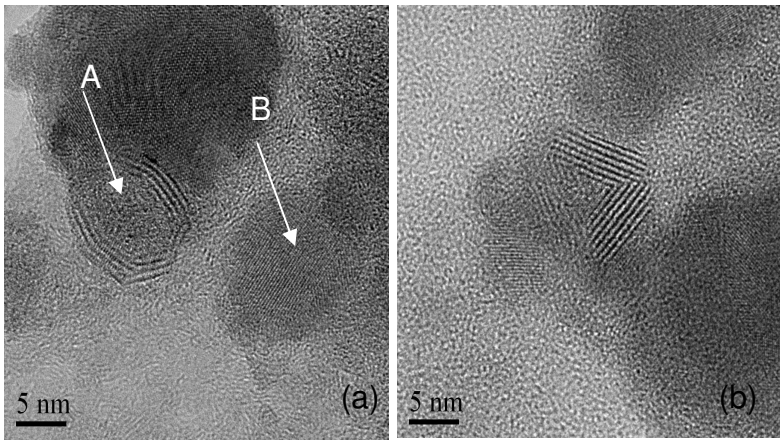

Fig. 41 (a) TEM image of MoS_2 (A) and MoO_3 (B) IF-nanostructures; (b) TEM image of MoS_2 nanostructure with different shape.

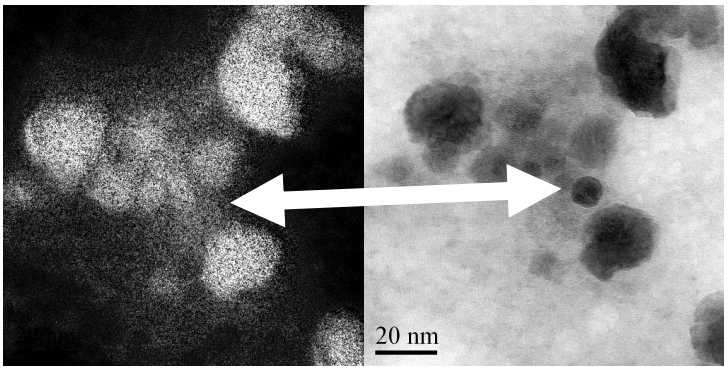

Fig. 42. Comparison between the elemental maps of Sulphur (a) and Molybdenum (b), showing a MoO_3 nanostructure.

The first (A) is unambiguously attributed to hollow fullerene-like MoS_2 clusters with a characteristic structure as those reported by other authors [125]. The main fingerprint for their individuation is the interlayer spacing (0.6 nm) and the characteristic polyhedral closed cage structure which is recognized to be thermodynamically more stable then isolated basal sheets of a sulphide lamellar structure [126]. Inside the cages a solid core seems to be present.

In some cases MoS_2 nanostructures with different shapes have been observed as well (Fig. 41b).

In this picture, a multiwalled nanostructure with a triangular shape is reported; in this case, the sulphide layers, with the same interlayer distance of 0.6 nm, are stacked to form flat planes instead of curved surfaces. This last kind of nanoparticle could be the result of the fragmentation process of the microcrystalline target or a successive size reduction due to laser irradiation process.

Such phenomena have been already observed during the irradiation of metallic targets and have been recognized as an active mechanism during LPLA at appropriate wavelengths [127].

Other particles with a completely different crystalline arrangement have been evidenced by TEM observations as that labelled with the letter B in Fig. 41a.

Lattice fringes are evidente in the image and suggest that the particle is a single crystalline MoO_3 cluster. This observation is at the same time obvious and intriguing. First of all it must be observed that during the ablation of the MoS_2 target by monosecond laser pulses the interaction of the front part of the laser pulse with the target creates vapours of the target surface, which are irradiated by the tail part of the same pulse. It causes

photoionization and the generation of a dense, high-temperature, and high-pressure laser plasma plume, which expands into the liquid. During this phase of expansion, plasma plume interacts with the surrounding liquid, creating cavitation bubbles, which, upon their collapse, give rise to extremely high temperature and pressure. In such a condition, dissociation of MoS_2 and water happens, giving rise to the presence of molybdenum ions and reactive oxygen species. In this conditions, the formation of a stable oxide specie such as MoO_3 is highly probable.

On the other hand, the conversion of MoO_3 nanoparticles into IF-MoS_2 has been extensively investigated [128].

The reaction path is generally divided into two distinguishable stages, namely a first surface reaction during which the surface oxide nanoparticle is converted into 1-2 closed monolayers of metal disulfide and a second step consisting in a slow diffusion of sulphur atoms from the vapour plume through the growing sulphide layers to the oxide core of the nanoparticle.

It must be noted that atomic diffusion rates vary exponentially with temperature, then the high temperature (several thousand of degrees) reached during the LPLA process dramatically shorten the time required to complete the reaction.

The conversion of molybdenum oxide into IF-MoS_2 implies the condensation of molecular Mo_3O_9 clusters into substoichiometric MoO_{3-x} nanosize particles, ready for the sulfidization.

From this complex picture and from the data available it is difficult to distinguish if the formation of IF-MoS_2 is due to a direct condensation of the atomic/molecular species in the plasma or it is

a multistep process which involves the synthesis of oxides or suboxides species.

Moreover, no one paper is present in literature that report specific informations about the bonding states and the chemical nature of the material produced either in the case of IF-MoS_2 synthesis by far-from-equilibrium processes (laser ablation, arc discharge and electron beam irradiation) or by chemical methods like chemical vapour transport.

With the aim to obtain a complete description of the chemical nature of the species obtained and to indicate a possible reaction route leading to the formation of IF-MoS_2 on the basis of experimental data, we performed a series of X-rays Photoelectron Spectra, described on the following.

XPS characterization

With the aim to obtain a complete description of the species produced in our experiment both from a structural and a chemical point of view, we performed a detailed XPS analysis of the sample, obtained by laser ablation of MoS_2 in water, drop-casted on a silicon substrate.

Fig. 43 shows the Mo_{3d} and S_{2p} XPS regions of the sample obtained together with the MoO_3 and MoS_2 spectra given as a reference.

As evidenced in the decomposition of the S_{2p} signal, three different sulphur-containing chemical species are present; the spectrum shows infact three 3/2-1/2 spin-orbit doublets, falling at 162.3-163.6 eV, 163.7-164.9 eV and 169.2-170.5 eV, respectively assigned to MoS_2, external sulphur and sulfates on the basis of

literature data [129]. It is worth noting that with the attribution of "external sulphur" we indicate both polysulfides and elemental sulphur since polysulfides signals and sulphur signals are not distinguishable in XPS on the basis of B.E. values.

Elemental sulphur could be present in our system in the form of linear chains with sulphate groups at the end of each chain. The presence of such a structure in aqueous solution has been reported by R. Steudel [130].

Mo_{3d} signal indicates the presence of a predominant quantity of Mo^{VI} and small quantities of MoS_2. On the basis of the B.E. values, the Mo^{VI} species we find can be assigned both to MoO_3 and to Mo oxysulphates. Therefore, XPS analysis describes a quiet complex picture related to the chemical composition of the material obtained. We find a small quantity of MoS_2 (few percent of the total Mo content), together with a high quantity of MoO_3 or MoO_2SO_4 which is largely predominant. As indicated by the TEM analysis part of the MoS_2 is present as crystalline nanostructures of different shapes.

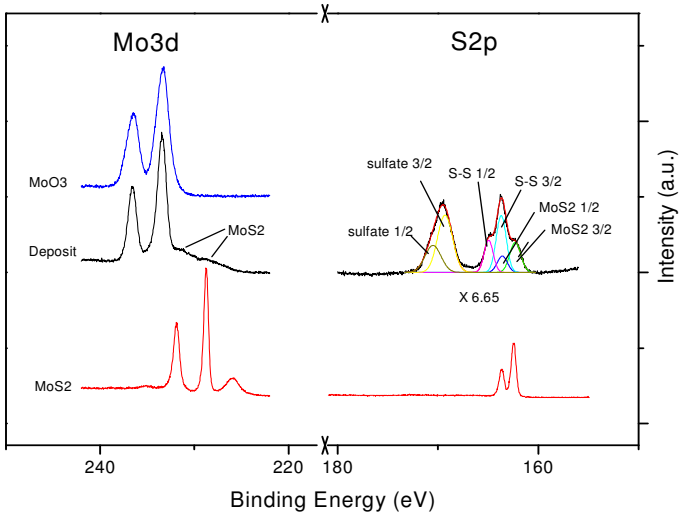

Fig. 43 Mo_{3d} and S_{2p} XPS regions of the deposit obtained (black line) together with MoO_3 (blue line) and MoS_2 (red line) reference spectra.

Indeed, literature studies report many sulphates and oxysulphates of Mo^{III}, Mo^{IV} and Mo^{VI} as stable products [131]. It is therefore reasonable to suppose that the two peaks visible in the region 222-240 eV result by the overlap of the Mo^{3d} components related to Mo^{VI} sulphates and oxysulphates.

It is worth noting that at lower B.E. values is visibile a large and weak shoulder, resulting by the overlap of the S_{2s} signals of the different sulphur species, of the Mo_{3d} signals related with MoS_2 and, probably, with different Mo suboxides as well ($MoO_{3-\delta}$ con $0 < \delta < 1$).

The intensities of the MoS_2 signals can be directly extimated on the basis of the intensity values of the MoS_2 S_{2p} signal:

$$I(Mo3d;MoS_2) = \tfrac{1}{2} I(S2p;MoS_2) \cdot \frac{RSF(Mo3d)}{RSF(S2p)}$$

In the same way it is possibile to estimate the intensity of the S_{2s} signals.

In this way it is possibile to obtain an approximative extimation of the molar ratio between the MoO_x molibdenum and MoS_2 molibdenum, that results around 7.

In order to verify the possibility to purify the samples obtained, in terms of content of sulphate, external sulphur and molybdenum oxides, we performed a thermal treatment under vacuum at six different temperatures. Fig.44a,b report the Mo_{3d} and S_{2p} signals of our sample at the different temperatures of annealing.

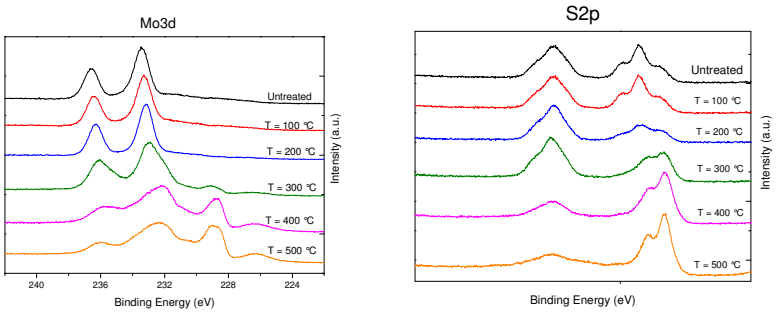

(a) *(b)*

Fig. 44: Mo3d (a) and S2p (b) XPS spectra of the samples obtained at different temperature of annnealing

The are many processes occurring when increasing the temperature. In the range between 25°C and 200 °C no significative variations are evidenced in the Mo_{3d} region. Also the components related to molybdenum sulphate and sulphide are nearly unchanged.

The only one important variation is represented by the intensity decreasing of the S°_{n} signals. What we observe indicates that up to 200 °C the only one relevant evidence is sulphur evaporation.

It is plain that at these temperature values the sulphur evaporation rate is strongly preponderant with respect to the reactions of reduction and sulphuration of the oxide [128]:

$$MoO_3 + \frac{x}{2} S \rightarrow MoO_{3-x} + \frac{x}{2} SO_2$$

$$MoO_{3-x} + \frac{7-x}{2} S \rightarrow MoS_2 + \frac{3-x}{2} SO_2$$

The thermal treatment at 300 °C leads the evaporation process of sulphur to its completion; at the same time, in the Mo_{3d} region, the $Mo_{3d\ 5/2}$ component related to MoS_2 becomes evident.

Finally, an asymmetric broadening (towards lower B.E. values) of the signals related to a Mo^{VI}-O suboxide is evident. These shoulders are assignable to the Mo_{3d} components of Mo^{V} and Mo^{IV} centers of the Mo_{3-x} suboxide.

On the basis of what we described, it is easy to deduce that in this temperature range the reactions of reduction and sulphuration of MoO_3 become competitive with respect to the residual sulphur evaporation process.

During annealing at 400 °C three relevant processes take place: decreasing of the sulphate amount, conversion of part of MoO_3 (and/or sulphoxide MoO_2SO_4) into suboxides MoO_{3-x} and the increase of the MoS_2 content.

The decrease of the sulphate signal could be explained by the reaction leading to the decomposition of MoO_2SO_4 at high temperature (~ 400 °C):

$MoO_2SO_4 \rightarrow MoO_3 + SO_3$

Indeed, our experimental evidences indicate that sulphate is the sulphur source required for the conversion of Mo oxide into sulphide, as it is obvious since $S°_n$ is nearly absent because it is completely evaporated. Actually, in our case sulphur produced during the sulphate decomposition does not lead to the production of SO_3 but is transferred to MoO_3 to obtain MoS_2.

In order to fully understand and clearly explain this complex picture, we have also to consider the presence of carbon, that plays a crucial role in the reactions that take place during the thermal treatment of our samples.

It is known in literature that the reaction between carbon and SO_x takes place even at 350 °C to produce sulphur:

$$C + SO_x \rightarrow S + CO_2(CO)$$

Therefore, we must consider all the reaction that take place in the same range of temperature:

- sulphate decomposition, to obtain SO_3
- Reaction of SO_3 with Carbon to obtain Sulphur
- Reduction and sulphuration of MoO_3 made by sulphur produced

A comprehensive representation of the chemical reactions involved is reported on the following:

$$9C + 4(MoO_2)SO_4 \rightarrow 2MoO_3 + 2MoS_2 + 9CO_2 \uparrow$$

Moreover, carbon can induce independently the MoO_3 reduction:

$$MoO_3 + \frac{\delta}{2}C \rightarrow MoO_{3-\delta} + \frac{\delta}{2}CO_2$$

In the thermal treatments above 400 °C we do not observe significative variations with respect with the situation described. Sulphur reaction we propose gives to completion and the reduction of MoO_3 goes on, leading to the increasing of Mo^V and Mo^{IV} components in MoO_{3-x} signal.

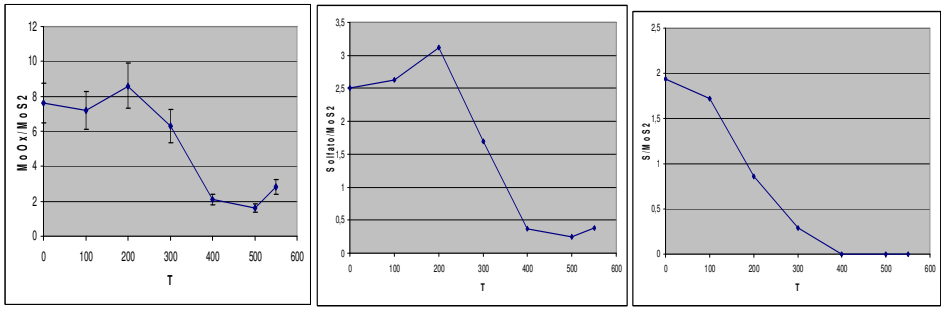

(a) *(b)* *(c)*

Fig. 45. Trends of the ratios MoO_3/MoS_2 (4a), Sulfate/MoS_2 (4b) and external sulphur/MoS_2 (4c) as a function of temperature.

Conclusions

The work done during the thesis allowed me to study in depth the many aspects of physical chemistry of the most innovative nanomaterials and to use the most important tools in spectroscopic and microscopic characterization of chemical, morphological and structural properties of nano systems.

The thesis, in part focused on carbon-based nanostructures, was structured initially considering HOPG graphite and graphene, and then studying the one-dimensional systems such as carbon nanotubes and polyynic nanowires.

XPS study on graphite HOPG, which has the aim to obtain the chemical and physical characterization of the two surfaces, basal and edge, led to the conclusion that the system has significant differences in the spectroscopic features of the two surfaces; in fact, while the basal plane is characterized by the presence of carbon sp^2 hybridized, highlighted by a study of the peaks C1s, the valence band and Auger signals, the surface edge shows a chemical composition that is not homogeneous, presenting, along with sp^2 signals, the presence of features characteristic of sp^3 systems. It is likely that the presence of "dangling bonds", with a high surface free energy content, due to symmetry breaking D6H system determined by the presence of the surface, leads to a rearrangement of the terminal carbon atoms in order to decrease to their free energy content, rearranging to a sp3 hybridization.

The study of graphene has been directed to the development of a new synthetic route for the production graphene nanoribbons,

using SWCNT as precursors rather than the most commonly used MWCNTs precursors. Both Raman spectroscopy and TEM images have confirmed the graphene nanoribbon structure of the synthesized carbon nanostructures. FT-IR and XPS analysis were used to determine the chemical functionalities of the graphene nanoribbons produced. This new synthetic approach demonstrates that the selective choice of the chemical precursors strongly influences the final morphology of the product, obtaining graphene nanoribbons.

By using atomic force microscopy we have determined the distribution of the lateral and vertical dimensions of the nanostructures on the graphene nanoribbons observed sample. A correlation between the island height and the island diameter is also observed.

The study of 1-D carbon nanostructures started with the production of carbon nanotubes by arc discharge in liquid nitrogen and comparing these structures with those produced by laser ablation. A comparison between these two strategies has shown that linear carbon chains are one of the most important products of any experimental condition either in the case of laser ablation or arc discharge. On the other hand, the formation of carbon nanotubes is mostly due to the presence of a strong driving force during the discharge at high current values. Some particular cases in the formation of these nanotubes is accompanied by the presence of tube-chain hybrids, during unstable discharge conditions.

The study of 1-D carbon nanomaterials continued with the study of the interaction between CNWs and noble metal surfaces. Polyynes adsorbed on noble metal nanoparticles present good

quality SER spectra polyyne indicating that the metal-surface interactions are more efficient for than silver for gold. Moreover the CNW-gold interaction leads to a single high wavenumber SERS signal, suggesting the hypothesis of chain dimerization that in the case of silver prevails. These findings could be Glaser correlated with a more efficient reaction in the case of silver as a consequence of the less availability of gold ions to give the necessary precursors for the reaction. This is confirmed by the invariance of the ITS PR signal upon incubation of gold nanoclusters with polyyne colloids.

Experiments conducted by protecting the metal surface with thiol SAMs allow to clear out the sp^2 spectral region and show the presence of an intermediate new peak between those present on bare metals, two to appearing as a dominant species. It is difficult to decide whether the presence of such an intermediate peak depends on a higher concentration of the relevant polyyne or if it is due to which species penetrated into the SAM layer, giving rise to a stronger effect for enhancement of both electromagnetic and chemical factors of the Raman amplification of signal. Finally, when a thermal treatment is carried out on samples polyyne adsorbed on silver, we ascertained that longer chains possesses lower thermal stability and tend to transform into amorphous species increasing the sp^2/sp intensity ratio.

In the second part of the thesis, on the nanostructured not carbon-based, I carried out the chemical characterization of one-dimensional nanostructures based on molybdenum, sulfur and iodine, indicated by MoSI. In particular, I studied the nature of

their interaction with nano particles of gold that is of exceptional importance for the production of network wires at the nanoscale.

I have also studied the production of fullerene-like MoS_2 nanoparticles by laser ablation in water, suggesting a possible reaction path leading from the target to the formation of polycrystalline MoS_2 nanoparticles.

The study of MoSI involved two different stoichiometries, indicated by 636 ($Mo_6S_3I_6$) and 644 ($Mo_6S_{4.5}I_{4.5}$). It is experimentally observed that the first system is the one that allows a better dispersion in organic solvent, and therefore a better purification, while the second is more aggregated in bundles. The characterization of products by mixing MoSI nanonetworks and gold nano particles produced by laser ablation in water showed that the interaction between gold and nanowires is through the sulfur end of the MoSI and through the link between gold and iodine atoms surrounding the nanowires.

In the study of MoS_2 fullerene-like systems obtained by laser ablation in water, it has been observed experimentally that these systems are produced through a multi-step process that includes a passage through the MoO_3 species.

References:

1. Kroto H.W. et al., Nature 1985, 318, 162
2. Iijima S. et al., Nature, 354, 56, 1991.
3. Kuzmany et al. Phys Stat. Sol. B 2006, 243, 2965
4. Zhang J.Z. Optical Properties and Spectroscopy of Nanomaterials, 2009, World Scientific
5. Ashby M. F. Nanomaterials, nanotechnology and Design, 2009, Elsevier
6. Sun B., Journal of Nanomaterials, 2010, 11, 402591
7. Tomiya et al. Surface and Interface Analysis, 2008, 40, 1677
8. Dresselhaus, MS et al. Science of Fullerenes and Carbon Nanotubes. Academic Press, (1996).
9. Forrò L. et al., Topics in Applied Physics, 2001, 80, 329
10. Matsuda Y. et al., Journ. Phys. Chem. Lett., 2010, 1, 2946
11. Ruoff R.S. et al. C.R. Physique, 2003, 4, 993
12. Avouris P.et al. Nature Nanotech., 2007, 2, 605
13. Fink H.W. et al. Phys. Rev. Lett. 67, 1543–1546 (1991)
14. Bekyarova E. et al., Journ. of Biomed. Nanotech., 2005, 1, 3
15. Dang T.X. et al., Journ. Struct. Biol., 2005, 150, 90
16. Wang Y. et al. Carbon, 2006, 44, 456
17. Cataldo F. Journ. of Raman Spectr., 2008, 39, 169
18. Cataldo F. Polyynes: Synthesis, Properties and Applications", CRC press, Taylor & Francis publishing group, Boca Raton, (2005)

19. Kolotilo D.M., Powd. Metall. and Met. Ceram., 1967, 7, 966
20. Ritter K.A. et al. Nature Materials, 2009, 8, 235
21. Bunch J.S. et al., Nanolett. 2008, 8, 2458
22. Flores M.Z.S. et al., Nanotech., 2009, 20, 465704
23. Patchkovskii S. et al., Proceed. Nat. Acad. Sci. Un. Stat. Am., 2005, 102, 10439
24. Du A., Journ. Am. Chem. Soc., 2010, 132, 2876
25. Jiang J.W. et al. Phys. Rev. B, 2009, 80, 113405
26. Meyer J.C. et al., Nature, 2007, 446, 60
27. Vrbanic D. et al. Nanotech., 2004, 15, 635
28. Bercic B. et al., Appl. Phys. Lett., 2006, 88, 173103
29. Kis A. et al., Adv. Mater., 2003, 15, 733
30. Nicolosi V. et al., J. Phys. Chem. B, 2005, 109, 7124
31. Mihailovic D., Prog. Mat. Sci., 2009, 54, 309
32. Van Attekum PMTM. Et al. Phys Rev Lett 1979, 43, 1896
33. Sette F. et al., Phys Rev B, 1990, 41, 9766
34. Yang D.Q. et al., Carbon, Langmuir, 2006, 22, 860
35. Balasubramanian T. et al., Phys Rev B, 2001, 64, 205420
36. Takata Y. et al., Phys Rev B, 2007, 75, 233404.
37. Smith R. et al., Phys Rev B, 2002, 66, 245409.
38. Hunt M., Phys Rev B, 2008, 78, 153408
39. Larsson K. et al. J Phys Chem, 1994, 98, 5019
40. Chen J.P. et al., Surf Sci, 1989, 216, 481
41. Ooi N. et al., Carbon 2006; 44: 231-42
42. Hu A. et al. Appl Phys Lett, 2007, 91, 131906
43. Titantah J.T. et al., Carbon, 2005, 43, 1311
44. Wang Y.Q., Chem. Mat, 2004, 16, 5427-36

45. Schafer J. et al., Phys Rev B, 1996, 53, 7762
46. McFeely F.R. et al. Phys Rev B 1974; 9(12):5268-78
47. Compagnini G. et al. Carbon, 1997, 35, 1793
48. Nakao A. et al. J Elect Spect, 1998, 88, 945
49. Buncick M.C. et al., Appl Surf Sci, 2000, 156, 97
50. Petukhov M.N. et al. Journ Chem Vap Dep, 1997, 5, 230
51. Novoselov et al., Science 2004, 306, 666
52. Novoselov et al. Proc Natl Acad Sci 2005,102,10451.
53. Castro Neto A.et al. Phys World, 2006, 19, 33
54. Katsnelson MI. Mater Today, 2007, 10, 20
55. Geim AK et al. Phys Today 2007, 60, 35.
56. Geim AK et al. Nat Mater 2007,6, 183.
57. Geim AK et al. Science 2009, 324, 1530.
58. Cataldo F. Carbon 2002, 40, 157.
59. Hashimoto A. et al. Nature 2004, 430, 870.
60. Elias DC et al. Science 2009, 323, 610.
61. Cricenti A. et al. Rev Sci Instrum, 1995, 66, 2843
62. Hummers WS et al. J Am Chem Soc 1958, 80, 1339.
63. Herold A et al. Mater Sci Forum 1994, 152, 281.
64. Valentini F. et al. Anal Chem 2003, 75, 5413.
65. Ferrari AC et al. Phys Rev Lett 2006, 97, 187401.
66. Compagnini G. et al. Carbon 2009, 47, 3201.
67. Pimenta MA et al. Phys Chem Chem Phys 2007, 9, 1276.
68. Cataldo F. Fullerene Nanot Carbon Nanostruct 2003, 11, 1.
69. Yang D et al. Carbon 2009, 47, 145.
70. Zhang G. et al. Carbon 2008, 46, 169
71. Li X. et al. Nat Nanotechnol 2008, 3, 538.

72. “Carbon Nanomaterials”, Y.Gogotsi edt, Taylor and Francis (London, 2006).
73. “Carbon Nanotubes”, M. S. Dresselhaus, G. Dresselhaus, Ph. Avouris Edts, Topics in Applied Physics 80, Springer (London, 2001).
74. Alexandrou I. et al. J. Chem.Phys, 2004, 120, 1055.
75. Compagnini G. et al. Chem. Phys. Lett., 1997, 272, 453 .
76. Compagnini G. et al. J. Mater. Res., 2001, 16, 2934.
77. Cataldo F. Tetrahedron, 2004, 60, 4265.
78. Heath . J. R. et al. J. Am. Chem. Soc., 1987, 109, 359.
79. Slepkov A. D. et al. J. Chem. Phys., 2004, 120, 6807.
80. Crljen Z. et al. Phys Rev Lett., 2007, 98, 116801.
81. Shashurin A. et al. Carbon, 2008, 46, 1792.
82. Compagnini G. et al. Appl. Phys. Lett., 1992, 61, 1796.
83. Ferrari A. C. et al. Phys. Rev. B, 2000, 61, 14095.
84. Calcagno L. et al. Nucl.Instr.Meth. B, 1996, 120, 121.
85. Gamaly E. G. et al. Phys Rev B, 1995, 52, 2083.
86. D’Urso L. et al. Carbon, 2006, 44, 2093.
87. Zhao X. et al. Phys. Rev. Lett., 2003, 90, 187401.
88. Scuderi V. et al. Carbon, 2009, 47, 2134.
89. Sakka T. et al. Appl. Surf. Sci., 2002, 197, 246 .
90. Kavan L., Kastner J. “Raman and infrared spectroscopy. In Carbyne and Carbynoid Structures”. Kluwer Academic Publisher, Dordrecht, 1999.
91. Nishide D. et al. J. Phys. Chem. C, 2007, 111, 5178.
92. Le Ru E. C. et al. J. Phys.Chem. 2007, 111, 13794.
93. Lee S. J. et al J. Phys. Chem. 2007, 111, 17985.

94. Compagnini G. et al. Phys. Chem. Chem. Phys. 1999, 1, 2351.
95. Kroto, H. W. et al. Nature 1985, 318, 162.
96. D'Urso, L. et al. Carbon 2006, 44, 2093.
97. Tabata, H. et al. Carbon 2006, 44, 3168.
98. Cataldo, F. Carbon 2003, 41, 2671.
99. Hu, A. Chem. Phys. Lett. 2008, 450, 375.
100. Crljen, Z. et al. Phys. ReV. Lett. 2007, 98, 116801.
101. Lucotti A. et al. Chem. Phys. Lett. 2006, 417, 78.
102. Compagnini G. et al. Phys.Chem. Chem. Phys. 2000, 2, 5298.
103. Mafune´ F. Chem. Phys. Lett. 2003, 372, 199.
104. Cataldo F. Carbon 2003, 41, 2671.
105. Pockrand I. Surface enhanced Raman vibrational studies at solid/gas interfaces. Springer tracts in modern physics; Springer: Berlin, 1984.
106. Manzel K. et al. Chem. Phys. Lett. 1982, 85, 183.
107. Wakabayashi T. et al. Chem. Phys. Lett. 2007, 433, 296
108. Compagnini G. et al. J. Raman Spectrosc. 2008, 39, 177.
109. Cataldo F. Carbon 1999, 37, 161.
110. Sortino S. et al. Angew. Chem., Int. Ed. 2002, 41, 1914.
111. Norrod K. L. et al. Anal. Chem. 1998, 70, 4218.
112. Casari C. S. et al. Appl.Phys. Lett. 2007, 90, 013111.
113. Mihailovic D. Prog. Mater. Sci. 2009, 54, 309.
114. Vrbanic D. et al. Nanotechnology, 2004, 15, 635.
115. Buttner M. et al. Thin Solid Films, 2006, 495, 180.
116. Koslowski B. et al. Surf. Sci., 2001, 475, 1.
117. Choy J. H. et al. J. Phys. Chem. B, 2003, 107, 3348.

118. Strle J. et al. Nano Lett., 2009, 9, 1091.
119. Grzelczak M. et al. Adv. Funct. Mater., 2008, 18, 3780.
120. Compagnini G. et al. J. Phys. Chem. C, 2008, 112, 20301.
121. Bissessur S. et al Chem. Mater, 1996, 8, 318.
122. Remikar M. et al. Adv Mater., 1998, 10, 246.
123. Margolin A. et al., J Mat Chem 2004, 14, 617.
124. Csaba L., J Phys Chem C, 2010, 114, 2421
125. Wiesel I. et al., Nano Res., 2009, 2, 416
126. Yin G.L. et al., Mat. Lett., 2007, 61, 1303
127. Zijie Y. et al., J Phys Chem C, 2010, 114, 3869
128. Yajima A. et al., Bull. Chem. Soc. Jpn., 1981, 3, 3759
129. Handbook of monochromatic XPS spectra, C.D. Wagner, Phys Electr.
130. R. Steudel et al. Top Curr Chem. 2003 230 153-166
131. Christiansen A.F. et al., Chem. Soc., Dalton Trans., 2001, 6, 806